

Measurement Criteria for the Magnetic Characterization of Magnetic Materials

Abdellahi Abderahmane¹ and Laurent Daniel¹, *Member, IEEE*

Abstract—Ferromagnetic materials exhibit nonlinear magnetic behavior, and many are anisotropic. Their magnetic characterization requires a mapping—in excitation and measurement—of the magnitude and direction of the magnetic field H or magnetic induction B . While many previous works have treated different parts of the characterization problem, the question of measurement reliability was not always adequately addressed. This work relies on key assumptions made in characterization experiments to propose three criteria that form a necessary and sufficient condition for reliable measurements: 1) material properties are assumed homogeneous in the measurement region (uniformity criterion); 2) measured H is assumed to be equal to that giving rise to the measured B (correspondence criterion); and 3) B & H directions are assumed known (direction criterion). Both theory and simulation are used to quantitatively assess the fulfillment of these assumptions using various apparatuses found in the literature along with new setup designs. Both alternating and rotating field loadings are considered for linear and nonlinear behaviors, using isotropic and anisotropic materials in both 1-D and 2-D excitation and measurement systems, with and without applied mechanical stress. The derived criteria are then used to establish guidelines for accepting, rejecting, and improving experimental apparatuses and offer clear insight into the measured data. In general, and when the application allows it, surface measurements of both B & H are recommended, 1-D excitation systems—though limited to certain applications—fulfill the criteria the most, and finally, while the excitation can be 1-D or 2-D, the measurement should always be 3-D.

Index Terms—Experimental characterization, magnetic measurement, magnetomechanical loadings, sample design.

I. INTRODUCTION

FERROMAGNETIC materials are used in various industrial applications. Understanding their behavior under different types of loadings (mechanical, electrical, magnetic, and thermal) helps improve the design and extend the lifespan of electromagnetic devices. This work deals mainly with the problem of magnetic characterization under applied magnetomechanical loading. Such a problem has been treated

Manuscript received 23 July 2023; revised 14 September 2023; accepted 20 September 2023. Date of publication 6 October 2023; date of current version 16 October 2023. This work was supported by the French Agence Nationale de la Recherche (ANR) under Grant ANR-22-CE42-0029-01 (project ENCORE). The Associate Editor coordinating the review process was Hamed Hamzehbahmani. (*Corresponding author: Abdellahi Abderahmane.*)

The authors are with CentraleSupélec, Centre National de la Recherche Scientifique, Laboratoire de Génie Electrique et Electronique de Paris, Université Paris-Saclay, 91192 Gif-sur-Yvette, France, and also with Centre National de la Recherche Scientifique, Laboratoire de Génie Electrique et Electronique de Paris, Sorbonne Université, 75252 Paris, France (e-mail: abdellahi.abderahmane@centralesupelec.fr; laurent.daniel@centralesupelec.fr).

Digital Object Identifier 10.1109/TIM.2023.3322510

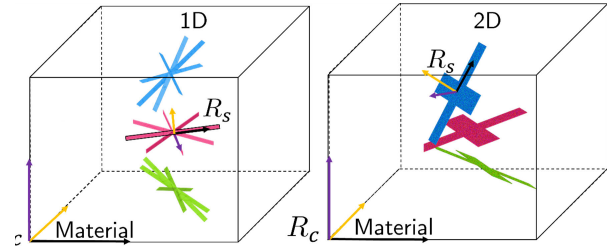


Fig. 1. Illustration of samples cut at various orientations with respect to the characterization reference frame R_c . On the left (resp. right), samples are used in 1-D (resp. 2-D) excitation and measurement systems. To each sample is attached a reference frame R_s .

both theoretically and experimentally by many authors in the literature ([1], [2], [3], [4], [5], [6], [7] to cite a few). However, to the best of our knowledge, no works have provided rigorous studies on the requirements for an experimental apparatus to yield reliable behavior identification. A characterization apparatus can generally be divided into the sample, the excitation, and the measurement systems. Characterization is carried out under the hypothesis that the sample's magnetic properties are homogeneous in the measurement region. In the case of a nonlinear behavior and an arbitrary anisotropy, the magnetic field H (or the magnetic induction B) must be applied and measured in a 3-D space. Two ways to do this are: 1) fixing the field magnitude and varying its direction (the rotating loading) or 2) fixing the direction and varying the magnitude (the alternating loading). Note, however, that an apparatus equipped with 3-D excitation and measurement parts and allowing the application of various loadings (e.g., mechanical or thermal) is challenging to design in practice, the reason being the difficulty of controlling the homogeneity and orientation of the 3-D loadings along with the instrumentation complexity. As a result, 1-D and 2-D excitation and measurement systems are often used. To compensate for the lost dimension(s), samples from the material are cut out at various orientations with respect to a characterization reference frame (denoted R_c). A reference frame R_s , attached to each sample (see Fig. 1), is needed to map the results back to R_c . All works found in the literature adopted such a procedure. A nonexhaustive list of such works is given hereafter.

Sievert [8] treats the induction and measurement of both alternating and rotating magnetic fields. Five configurations are studied. In three of them, two ferromagnetic yokes are placed on either side of the sample (a steel sheet) to channel the magnetic flux. The excitation coil is wound around the sample. In the first, 1 B-coil (wound around the sample

section) and 1 H-coil (on one side of the sample) are used to measure \mathbf{B} and \mathbf{H} . In the second, \mathbf{H} is measured using the magnetic path length and, in the third, a Rogowski coil. The fourth configuration has one yoke but two H-coils to compensate for the loss of symmetry (see [9] for details). The fifth configuration uses a square sample placed between four yokes with an excitation coil wound around each yoke. Here, an H-coil is used, and two sets of B-needles are used to measure \mathbf{B} (details on the H-coil and the apparatus can be found in [10]). Zurek and Meydan [11] treated the problem of magnetic losses for conventional oriented and nonoriented electrical steels under a rotating magnetic field. The apparatus used a disk sample placed in a round magnetizing yoke. The sample was magnetized using two orthogonal coils. To measure \mathbf{B} , two orthogonal B-coils were wound through small holes drilled in the sample. The same apparatus was used in another experiment [12], wherein the goal was to compare the power losses under controlled \mathbf{H} and controlled \mathbf{B} . Here, a 2-mm air gap was left between the yoke and the sample. Holes for the B-coils were drilled 20 mm apart, and the H-coil (in contact with the sample surface) was 20 mm wide. Stranges et al. [13] studied the possibility of predicting rotational power losses from alternating ones in nongrain- and grain-oriented steels. The apparatus used in this experiment is similar to the fifth configuration in [8] and that of Brix et al. [14]. Here, however, holes were drilled in the sample to wind B-coils. Ramos and Girão [15] used a similar apparatus to that of Stranges and Findlay [13], with the difference of using a cross-shaped sample. The particularity of Geirinhas Ramos and Silva Girão [15] work resides in measuring \mathbf{B} by winding around the sample legs while measuring \mathbf{H} (with an H-coil) at the sample center. Mori et al. [16] used finite element simulation to design an apparatus where various slits are made in the yokes to improve the field's uniformity. The sample consisted of a square-shaped steel sheet placed between two pairs of yokes. The excitation coils (orthogonal to each other) are wound around the sample. B-needles and H-coils were used to measure \mathbf{B} and \mathbf{H} . Ivanyi et al. [17] studied the case of a hexagonal-shaped sample. Six magnetizing yokes were used, and an air gap was left between the sample and the yokes. The types of sensors used for \mathbf{B} and \mathbf{H} measurements were not disclosed. The works presented herein give a broad overview of the types of apparatuses used for stress-free magnetic characterization. Other works [18], [19], [20], [21] have treated the same problem; however, the apparatuses used are similar to the ones previously referred to. An apparatus capable of 3-D excitation and measurement was treated in [22], consisting of 3-D coil systems for both the excitation and the measurement. Due to its design, the apparatus does not allow the application of mechanical stress.

Thus far, the sample was subjected to only magnetic loading. The problem where both magnetic and mechanical loadings are considered adds to the complexity due to the strong magnetomechanical coupling in ferromagnetic materials [1], [2]. Such a problem can be split into two categories: 1) uniaxial (the applied uniaxial stress is in the direction of the applied magnetic field) and 2) multiaxial (multiaxial stress is applied or the uniaxial stress is not in the direction of

the applied magnetic field). The uniaxial problem does not generally suffer from stress nonuniformity and was the subject of numerous works [23], [24], [25], [26], [27], [28], [29], [30], [31], [32], [33], [34], [35]. The sample shapes can be parallelepipedal [23], [27], [28], [32], [35] or cylindrical [31]. \mathbf{B} is measured using a B-coil wound around the sample cross section, and \mathbf{H} , using an H-coil [27], a Hall sensor [28], or a magnetic incremental permeability sensor [30]. The excitation coil can be wound around the sample [24] or the yokes [28]. Both isotropic [26] and anisotropic [24] materials were studied in the elastic [35] and plastic [25], [30], [35] regimes for low [32] and high [31] frequencies. In contrast, far fewer works treat the multiaxial problem, and they deal mainly with in-plane biaxial loading. Nevertheless, some works [36], [37], [38] can be found where the magnetic field is applied in a direction different from that of the applied uniaxial stress. In [36], only a single C-yoke—that can be rotated—was used. The residual magnetic induction was measured as a function of applied stress using a tunneling magnetoresistance (TMR) sensor. In [37], compressive stress was normal to the sample surface, while \mathbf{B} and \mathbf{H} were in the plane. An H-coil was used to measure \mathbf{H} , and a flux density sensor was used to measure \mathbf{B} . Like the uniaxial case, this kind of multiaxial magnetomechanical problem does not generally suffer from significant stress nonuniformity if these aspects are adequately addressed during the design of the sample. A study on stress uniformity in cross-shaped samples of various geometries subjected to uniaxial and biaxial loadings can be found in [39]. Langman [40] studied the effect of uniaxial and equibiaxial loadings on magnetic properties using a cross-shaped sample and a single C-yoke. The stress is introduced through bending. Sablik [41] treated a similar problem wherein the excitation coils were wound around the legs of a C-yoke placed on top of the sample. \mathbf{H} was measured using a Hall sensor placed between the legs, and \mathbf{B} was measured using a search coil wound around one leg of the C-yoke. Similar to previous work, Rekik et al. [42] used a cross-shaped sample and a single C-yoke. However, here, \mathbf{H} was measured using an H-coil and \mathbf{B} , using B-needles. A cross-shaped sample with slits in its arms—to have a more uniform stress distribution—was also used by Kai et al. [43]. Excitation coils were wound around the sample arms, and B- and H-coils were used for \mathbf{B} and \mathbf{H} measurements. A six-arm sample was used by Aydin et al. [44]. Such a sample allows the application of stress in an arbitrary in-plane direction. Excitation coils were wound around six separate yokes—forming the sides of a hexagon, whose diagonals are the sample's arms. \mathbf{H} was measured using an H-coil, and \mathbf{B} was measured using B-coils positioned through drilled holes. Finally, Kai et al. [45] used an eight-arm sample with slits in the arms to study the effect of shear stress on magnetic properties. The excitation coils were wound around two yokes, and \mathbf{B} and \mathbf{H} were measured using a vector-hysteresis sensor. These findings are summarized in Table I.

Though there is no shortage of experimental data in the literature, there seems to be no rigorous study assessing the reliability of experimental apparatuses. Such a study is the subject of this work, wherein a set of three criteria that allow for accepting, rejecting, improving an experimental apparatus,

TABLE I

SUMMARY OF SOME EXPERIMENTAL APPARATUSES FROM THE LITERATURE USED FOR THE MAGNETIC CHARACTERIZATION OF MAGNETIC MATERIALS. THE FIRST COLUMN(S) GIVES THE TYPE OF PROBLEM TREATED (STRESS-FREE, UNDER UNIAXIAL OR BIAXIAL MECHANICAL STRESS). THE SECOND COLUMN GIVES THE CORRESPONDING REFERENCE NUMBER. THE THIRD, THE SAMPLE SHAPE, THE FOURTH, AND THE EXCITATION COIL (WOUND AROUND THE YOKE(S) OR THE SAMPLE). THE FIFTH AND THE SIXTH GIVE **B&H** SENSORS. ABBREVIATIONS OF THE SAMPLE, EXCITATION COIL (EC), AND **B&H** SENSORS ARE GIVEN IN THE LAST ROWS

Problem	Ref	Sample								EC		B			H					
		Ss	Rs	Disc	R od	S p	C s	6 A	8A	Y	S	BN	BC	TM R	HS	HC	RC	MPL		
Magnetic	8	•	•							•	•	•	•			•	•	•		
	9		•								•		•			•				
	10		•							•			•			•				
	11			•						•			•			•				
	12			•						•			•			•				
	13	•								•			•			•				
	14						•			•			•			•				
	15						•			•			•			•				
	16	•								•	•	•		•		•				
	18			•						•			•			•				
	19		•			•				•		•			GMR					
	20		•								•		•			•				
21		•							•			•			•					
22	Cubic								•			•			•					
Magneto-Mechanical	Uniaxial	$(\sigma \parallel H)$	23				•				•			•			•			
			24				•	•			•	•		•			•			
			25				•					•		•			•			
			27					•				•		•			•			
			28				•	•				•		•			•			
			29		•							•		•			•			
			30		•								•		•					•
			31					•				•			•			•		
			32						•			•			•			•		
	33		•							•			•		•	μ_{inc} sensor				
	34		•							•			•		•					
	35						•			•			•		•					
	Multiaxial	$(\sigma \nparallel H)$	36				•				•			•					•	
37							•			•			•			•				
Biaxial		40						•			•			•						
		41						•			•			•						
		42						•			•			•						
		43						•			•			•						
44							•		•			•								
45								•	•			•								
Abbreviation		Ss: square sheet	Rs: Rectangular sheet		Sp: Slender parallelepiped		Cs: Cross shape		6A: six arms		EC: excitation coil									
	Y: Yoke	S: Sample	BN: B-Needle	BC: B-Coil	HS: Hall Sensor	HC: H-Coil	RC: Rogowski-Coil	MPL: Magnetic Path Length												

and providing clear insight into the measurements is proposed. These criteria are derived from the underlying assumptions made—but usually not explicitly established nor verified—in every magnetic characterization experiment: 1) the material magnetic properties are homogeneous in the measurement region [uniformity criterion (UC)]; 2) the measured magnetic field **H** is equal to the one giving rise to the measured

magnetic induction **B** [correspondence criterion (CC)]; and 3) **B&H** directions are known throughout the experiment time [direction criterion (DC)].

These criteria also apply to stress and strain and become even more urgent to meet for the magnetomechanical problem due to the strong coupling. This work shows, theoretically and through the simulation, that the proposed criteria form a

necessary and sufficient condition for reliable magnetic characterization. Numerous practical cases dealing with different materials, loading types, sample geometries, excitation, and measurement systems are studied. The criteria are then used to derive general guidelines that can be followed to improve both apparatus design and data interpretation. These include: 1) having the **B&H** measurement regions as close to each other as possible, preferably coinciding with the sample surface and 2) always carrying out 3-D measurements.

This article is organized as follows. Section II provides mathematical proof of the measurement criteria's necessity and sufficiency. Section III deals with the fulfillment of the criteria. Various cases are studied: 1-D (resp. 2-D) excitation systems are treated in Section III-A (resp. Section III-B) for both isotropic and anisotropic materials, with and without applied mechanical stress under alternating and rotating magnetic fields. Section IV is the conclusion. Throughout this article, bold notation is used for vectors and tensors.

II. THEORY

This section demonstrates the necessity and sufficiency of the three criteria defined in the introduction. In this work, the homogeneity assumption (i.e., with no loading, magnetic properties are assumed homogeneous within the measurement region) is maintained. All three criteria are independent of time and, thus, apply to both anhysteretic and hysteretic behaviors.

A. Uniformity Criterion

To single out the question of uniformity, **B&H** measurements regions are assumed to coincide, and their directions (at any point) are known. **B&H** sensors have finite volumes; ergo, their output is an average over a given region. The UC (i.e., the homogeneity hypothesis should be respected) assesses whether the averaging operation yields the material behavior. Without loss of generality, the magnetic behavior can be described by the following equation [1]:

$$\mathbf{B} = f(\mathbf{H}) = \boldsymbol{\mu}(\mathbf{H}) \cdot \mathbf{H}. \quad (1)$$

$\boldsymbol{\mu}$ is the magnetic permeability; it can be a tensor or a scalar. The permeability also depends on other factors, such as the crystallographic structure and applied or residual stress. Call V the measurement region volume; the measured **B&H** in this volume (denoted \mathbf{H}^m & \mathbf{B}^m) are found by integrating over the volume as follows:

$$\mathbf{H}^m = \frac{1}{V} \int_V \mathbf{H}(X) dV, \quad \mathbf{B}^m = \frac{1}{V} \int_V \mathbf{B}(X) dV. \quad (2)$$

For each spatial point X in V , the relationship $\mathbf{B}(X) = f(\mathbf{H}(X))$ is verified. Since $\boldsymbol{\mu}$ (representing the magnetic properties) depends on \mathbf{H} , which, in turn, depends on the position X , the validity of the homogeneity hypothesis (which would imply $\mathbf{B}^m = f(\mathbf{H}^m)$) in V is not always guaranteed. To assess such validity, V is discretized into N small elementary volumes v_n . The size of v_n is chosen so that \mathbf{B} , \mathbf{H} , and $\boldsymbol{\mu}$ are—practically—uniform and are denoted \mathbf{B}_n , \mathbf{H}_n , and $\boldsymbol{\mu}_n$. Equation (2) writes

$$\mathbf{H}^m = \frac{1}{V} \sum_{n=1}^N v_n \mathbf{H}_n, \quad \mathbf{B}^m = \frac{1}{V} \sum_{n=1}^N v_n \mathbf{B}_n. \quad (3)$$

Since, in v_n , the quantities \mathbf{B}_n , \mathbf{H}_n , and $\boldsymbol{\mu}_n$ are uniform (i.e., independent of the position X), the relationship $\mathbf{B}_n = f(\mathbf{H}_n) = \boldsymbol{\mu}_n \cdot \mathbf{H}_n$ is also verified. Substituting \mathbf{B}_n in (3) yields

$$\mathbf{B}^m = \frac{1}{V} \sum_{n=1}^N v_n f(\mathbf{H}_n). \quad (4)$$

The following relationship:

$$f(\mathbf{H}^m) = f\left(\frac{1}{V} \sum_{n=1}^N v_n \mathbf{H}_n\right) = \frac{1}{V} \sum_{n=1}^N v_n f(\mathbf{H}_n) = \mathbf{B}^m \quad (5)$$

is true *if and only if* the function f is linear for all $\mathbf{H}(X)$ where $X \in V$. Note that, since \mathbf{H} is a vector, f needs to be linear for both the field magnitude and direction. As a result, nonuniformity—in field direction and magnitude—does not affect isotropic materials exhibiting linear behavior. For isotropic materials with nonlinear behavior, its effect is minimal around saturation (where the behavior is relatively linear) and maximal around the knee of the $B(H)$ curve (norm of \mathbf{B} as a function of the norm of \mathbf{H}). The effect on anisotropic linear or nonlinear materials depends on the type of anisotropy. In conclusion, high nonuniformity does not always equate to high error. For convenience, nonuniformity in the measurement region can be split into: 1) through-thickness and 2) in-plane. To minimize the effect of the first, the excitation frequency can be decreased to reduce the effect of eddy currents until measurements are no longer dependent on it. For the second, the region on which the measurements are averaged can be reduced (it needs, however, to be large enough to be representative of the material).

B. Direction Criterion

To single out the question of direction, **B&H** measurements regions are assumed to coincide, and their distributions (magnitude and direction) are uniform. **B&H** sensors measure the projections of fields in one, two, or three directions. Since the field's direction and magnitude cannot, in general, be deduced from one or two projections, the DC (**B&H** directions should be known) becomes mandatory. To prove this, call (θ_B, ϕ_B) and (θ_H, ϕ_H) the angles defining **B&H** directions in R_s (the sample reference frame). Consider the case where only single-axis (one projection) sensors are used to measure **B&H**. Without loss of generality, these sensors are assumed to measure the components in the x -direction (i.e., B_x & H_x). Consequently, the $B = f(H)$ curve is now replaced by the curve $B_x = f(H_x)$. Since $B_x = \sin(\theta_B) \cos(\phi_B) B = k_B B$ and $H_x = \sin(\theta_H) \cos(\phi_H) H = k_H H$, the equation $B_x = f(H_x)$ is now rewritten as

$$B = \frac{1}{k_B} f(k_H H). \quad (6)$$

In the case where $\mathbf{B} \parallel \mathbf{H}$ one has $k_B = k_H$ as a result, the $B_x = f(H_x)$ curve is the image of the $B = f(H)$ curve under a pseudohomothety of coefficient k_B . Such transformation is not a real homothety since $k_B = \sin(\theta_B) \cos(\phi_B)$ depends on the direction of \mathbf{B} . If, on the other hand, $\mathbf{B} \nparallel \mathbf{H}$, $B_x = f(H_x)$ is a distorted image of that of $B = f(H)$ (i.e., shrinking

the H -axis with k_H and the B -axis with k_B). This result is generalized to the 2-D case where double-axis sensors (two projections) are used (here, $k_B = \sin(\theta_B)$ and $k_H = \sin(\theta_H)$). In conclusion, the field directions should be known; otherwise, the 1-D and 2-D measurements can yield distorted images of the real behavior. Such directions can be known in practice by measuring in three orthogonal directions (the out-of-plane B component can be measured using the continuity of the normal magnetic induction component boundary condition).

C. Correspondence Criterion

To single out the question of correspondence, B & H distributions (magnitude and direction) are uniform, and their directions are known. The CC stipulates that the measured H should correspond (be equal) to the one giving rise to the measured B . Such a criterion is necessary for two reasons: 1) the measurement regions of B & H are generally distinct (B is measured within the material volume while H outside the material volume) and 2) since B & H are vectors, the orientations of their corresponding sensors are needed to define them uniquely. The consequence of 1) is that the measured magnetic field (call it H^m) is generally different (in magnitude and direction) from the magnetic field (call it H), giving rise to the measured B^m . The relationship between the two can be written as follows: $H^m = A(\mu) \cdot H$, where A is a 2×2 tensor that depends on the experimental apparatus and the material properties. As a result, not respecting the CC compromises the reliability of all measurements—except the ones involving only B . In practice, to overcome such an issue, B & H measurement regions should coincide or at least be as close to each other as possible. Such a condition is met when H measurement is carried out at the sample surface (assuming a through-thickness uniformity). It is worth emphasizing that, when both B & H are measured at the surface, through-thickness uniformity is not mandatory. As a result, measurements can be carried out at relatively higher frequencies.

To study the effect of misorientation (2), B & H measurement regions are chosen—without loss of generality—to coincide. Two cases can be distinguished.

- 1) No misorientation is present between B & H sensors; however, there is one between the sensors and the sample reference frame R_s . In this case, isotropic materials are unaffected since, to such materials, R_s orientation—with respect to the characterization reference frame R_c —is of no importance. As for anisotropic materials, this translates to the measured material properties to be the image of the real ones under the rotation $\text{rot}(R_s \rightarrow R_B)$, where R_B is the reference frame attached to the B sensor.
- 2) R_s , R_B , and R_H (the reference frame attached to the H sensor) all have different orientations with respect to R_c . Let C_{BH} be the direction cosines matrix between R_B and R_H (i.e., the product of the three rotation matrices around R_B -axes). For isotropic materials, the constitutive relation $B(H)$ becomes $B = \mu(H)[C_{BH} \cdot H]$. The fact that the norm of $C_{BH} \cdot H$ is equal to H shows that measurements involving only the field norms are unaffected.

TABLE II
MATERIAL PROPERTIES

Properties	Yoke	Sample	Coil
ϵ [F/m]	ϵ_0	ϵ_0	ϵ_0
σ [S/m]	1	Case dependent	$6e7$
μ [H/m]	$1e4/8e4$	Case dependent	1

In addition, measurements involving only each of the fields alone (e.g., $B_y(B_x)$, $B_z(B_x)$, $H_y(H_x)$, $H_z(H_x)$...) are also unaffected. However, those mixing the fields (e.g., $B_x(H_x)$, $B_y(H_y)$...) are affected since they depend on the components of C_{BH} . Due to the presence of C_{BH} (i.e., a tensor), the fields B & H are now non-collinear for isotropic materials. This observation shows that such materials can, in principle, be used in a calibration step to gauge misorientation between these sensors. As for anisotropic materials, only the measurements, including the fields' norms, remain unaffected.

The misorientation between sensors differs from the one given by 1) because material properties are not the images of the real ones under any rotation. This is because misorientation between R_B and R_H can render noncollinear fields collinear and vice versa. In practice, isotropic materials can be used in a calibration step to reduce sensor misorientation.

In summary, the three-criteria fulfillment is necessary for reliable magnetic characterization. If not guaranteed, various errors that add to or subtract from each other can emerge. When all three criteria are combined, they form a sufficient condition. This is evident since their combination yields a known and unique load (H) and material response (B), which corresponds to each other. Section III assesses the fulfillment of the criteria derived herein for various types of apparatuses using simulation. Though these criteria apply to hysteretic and anhysteretic behaviors, simulations were carried out under the latter.

III. SIMULATION

The fulfillment of the B & H measurements' criteria (BHmC) is assessed through various studies. Both alternating and rotating field loadings are considered for isotropic and anisotropic materials in 1-D and 2-D excitation systems, with and without applied stress. In all studies, currents are imposed. All apparatuses have one sample, yokes, and excitation coils (material properties given in Table II).

While studies were carried out for both linear and nonlinear behaviors, the results shown here correspond to the latter. However, conclusions from the linear cases are recalled if need be. Unless specified otherwise, the excitation frequency and samples' thickness (10 mHz and 2 mm in all cases) are chosen to achieve through-thickness uniformity for all studied materials. In practice, B & H sensors output voltage signals from which the field magnitude and direction are inferred. To avoid errors due to sensor design and precision, points, surfaces, and volumes are used in this section to model the sensor's effective area. For each study, one or more of the following six results are presented: 1) the real

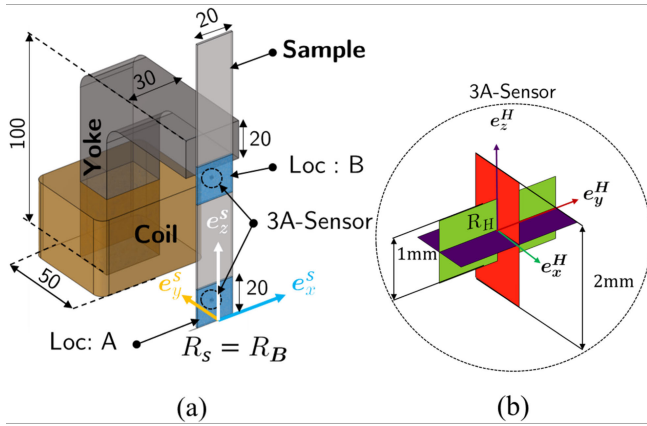


Fig. 2. Typical apparatus used for 1-D characterization (all dimensions are in mm). (a) One-quarter of the apparatus. (b) Zoom-in on the triple-axis sensor (3A-sensor) used for \mathbf{H} field measurement. R_H is the reference frame attached to the 3A-sensor and is centered at 1.5 mm above the surface.

material behavior; 2) measurements at a single point (all three criteria are met); 3) at the sample surface (the UC is not necessarily met); 4) above the sample surface with no misorientation and with triple-axis sensor (only orientation criterion is met); 5) with \mathbf{B} & \mathbf{H} sensors misorientation (only orientation criterion is met); and 6) with single- or double-axis sensors but without misorientation (all three criteria are not met). Further complementary results and conclusions from studies not shown (due to lack of space) particular to each case shall be provided for clarity. All simulations are carried out using COMSOL Multiphysics.¹ For each study, the mesh type (resp. size) was systematically adapted (resp. refined) to have accurate results (i.e., independent of the mesh).

A. 1-D Systems

A typical apparatus used for 1-D characterization is presented in Fig. 2. Only one-quarter of the apparatus is shown [see Fig. 2(a)]. Such apparatus can be used to characterize both isotropic and anisotropic materials. The BHmCs are tested first for the isotropic case.

Each \mathbf{H} field component is averaged over the corresponding $1 \times 2 \text{ mm}^2$ plate (which represents the effective area of a Hall sensor). R_H is centered at 1.5 mm from the sample surface. For this 1-D system, R_B coincides with R_S . The \mathbf{B} measurement region is represented by a blue parallelepiped, over which the \mathbf{B} field norm or B_z component is averaged (which emulates the effective area of a B-coil, wound around the sample section).

1) *Isotropic Materials:* For the present case, characterization is carried out at two locations. The first (denoted Loc: A) is close to the sample center, and the second (denoted Loc: B) is close to the yoke end (see Fig. 2). In Fig. 3(a), “BH” (dot marker) gives the real magnetic behavior of the sample material (i.e., the $B(H)$ curve used to run the simulation). “Point” (solid black line) gives $B = f(H)$ at a single point (inside the sample) in the blue region. “Surface” (“x” marker) gives $\text{avg}(B) = f(\text{avg}(H))$ at the sample surface. “3A” (green solid line) gives $\text{avg}(B) = f(\text{avg}(H))$, where \mathbf{B} is averaged over the blue volume and \mathbf{H} is measured using the

3A-sensor [see Fig. 2(b)]. “1A-surface” (circular marker) gives $\text{avg}(B_z) = f(\text{avg}(H_z))$ at the sample surface. “1A” (diamond marker) gives $\text{avg}(B_z) = f(\text{avg}(H_z))$, where the average of H_z is measured using a single-axis sensor [i.e., one plate of the 3A-sensor given in Fig. 2(b)]. Finally, “1A-Mis” (square marker) gives $\text{avg}(B_z) = f(\text{avg}(H'_z))$, where H'_z is given by $H'_z = (\mathbf{C}_{H \rightarrow S} \cdot \mathbf{H}) \cdot \mathbf{e}_z^H$ ($\mathbf{C}_{H \rightarrow S}$ is the direction cosines matrix between the sample reference and that of the \mathbf{H} field sensor). In this example, $\mathbf{C}_{H \rightarrow S}$ is the rotation matrix of a 30° angle around the \mathbf{e}_y^S -axis. Other studies used smaller misalignments (2.5° , 5° , 10° , 15° , and 20°). Their deviations, however, were small, making them visually tricky to distinguish from the real material behavior and, thus, the choice of the larger 30° angle. At loc-A, all results, except the one with misorientation, practically coincide with the real material behavior. The reason for this is that, at loc-A, both \mathbf{B} & \mathbf{H} fields are practically in the \mathbf{e}_z^S -direction (i.e., along the sample length). This is shown in Fig. 3(c), where the direction cosines ($100H_i/H$ and $100B_i/B$ denoted X where $i \in \{x, y, z\}$) are given as a function of the experiment time. The small nonnull H_y component at this location was shown—in a separate simulation—to depend on the distance between the sample and the 3A-sensor. Fig. 3(b) gives the same results but at location B. Only the results corresponding to the single point measurement (taken at the center of the blue region at location B and where all BHmCs are respected) coincide with the real material behavior. The coincidence between “Surface” and “1A-surface” shows that both fields at the surface are in the z -direction, which shows that the deviation from the real behavior is due to an ill-respected UC. At this location, the result with misorientation is closer to the real material behavior than that without it (square marker). The same is true for the result using a single-axis sensor (diamond marker) compared to that using a 3A-sensor (solid green line where the error can be 80%). This observation confirms that errors emerging from ill-respected BHmC can add to or subtract from each other. Fig. 3(c) shows that, at this location, the \mathbf{H} field changes its direction throughout the experiment, which can only be detected when carrying out 3-D measurements. To showcase the effect of the through-thickness nonuniformity—thus far guaranteed due to the low frequency (10 mHz)—location A is chosen for the measurement at different frequencies. Besides the real material behavior (dot marker), Fig. 3(d) gives measurements for 100 and 500 Hz. In all three curves, the \mathbf{B} field norm ($\approx B_z$) is measured in the material volume, the \mathbf{H} field is measured at the surface (100 and 500 Hz:H-S) and above the surface at the 3A-sensor position (500 Hz:H-3A). Note how measurements strongly depend on the frequency. Since in-plane uniformity is guaranteed at location A (this was also verified here), the deviations of 100 and 500 Hz:H-S from the real material behavior are solely due to through-thickness nonuniformity. The deviation of 500 Hz:H-3A results from both an ill-respected uniformity and correspondence criteria. Note how close to saturation the curves at high frequencies coincide with $B(H)$. This is due to the low permeability around saturation, which yields a large skin-depth and, thus, a better through-thickness uniformity. Finally, the curve corresponding to measurements at the surface for both \mathbf{B} & \mathbf{H} (not shown

¹Trademarked.

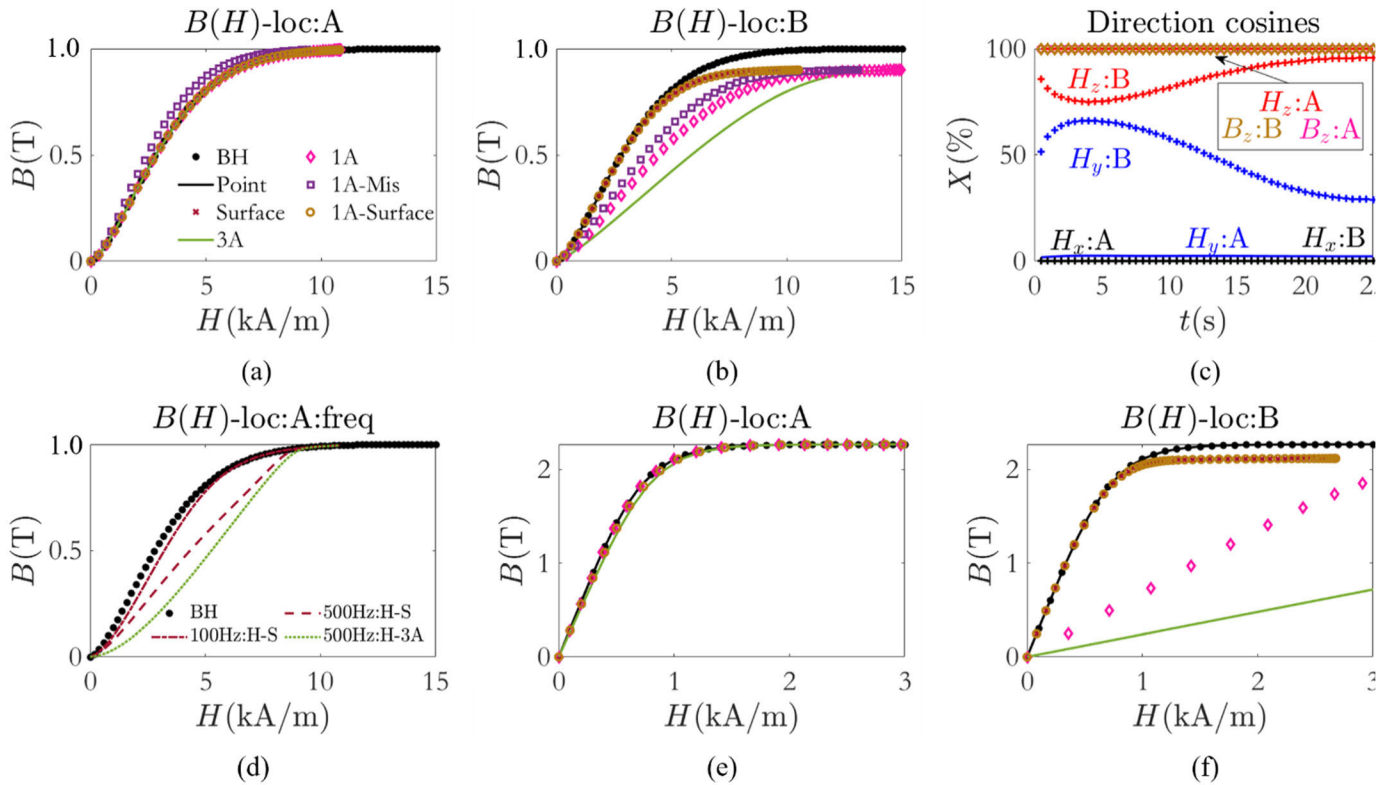


Fig. 3. (a) [resp. (b)] Measurement carried out at location A (resp. B). Dot marker: the real material behavior. Point: measurements (of both \mathbf{B} & \mathbf{H}) at a single point inside the sample. Surface: measurement (of both \mathbf{B} & \mathbf{H}) at the surface. 3A: \mathbf{B} is measured in the sample and \mathbf{H} above the sample using the 3A-sensor. 1A: like 3A; here, however, only a single-axis sensor is used for \mathbf{H} . 1A-Mis: measurements with 30° \mathbf{B} & \mathbf{H} misalignment. 1A-surface: similar to 1A; however, only B_z is used instead of the norm of \mathbf{B} . (c) gives the direction cosines of both vectors \mathbf{B} & \mathbf{H} ($100H_i/H$ and $100B_i/B$) in the sample reference frame. In (c), \mathbf{H} components at location A are given by solid lines and at B by “+” markers. (d) Measurements at different frequencies (100 and 500 Hz): \mathbf{B} is measured in the volume while \mathbf{H} at the surface (H-S) and above the surface (H-3A). (e) and (f) Same as (a) and (b) but for a different material.

for clarity) was shown to coincide with real material behavior. The dependence of the fulfillment criteria on the sample material properties is shown in Fig. 3(e) and (f) wherein a different material is used. Such dependence is evidenced by how large the discrepancies at location-B are, compared to those of the first material [see Fig. 3(b)].

Conclusions from complementary studies with different yoke permeabilities (1000 and 80000) and various sample materials (including those used in the 2-D systems case) are identical to the ones presented herein. In summary, location A is better for this apparatus and can be improved by moving the \mathbf{H} sensor close to the sample surface and, if possible, carrying out both \mathbf{B} & \mathbf{H} measurements at the surface. Furthermore, these results show that some configurations found in the literature [15] and [41] should be avoided: 1) measuring close to the yoke ends and 2) having the \mathbf{B} & \mathbf{H} measurement regions far apart. These two imply that measuring \mathbf{H} using the magnetic path length [32], [36] is inadequate since BHmC is hardly respected. Finally, measurements using a B-coil while there is through-thickness nonuniformity should be avoided. Studies wherein the 3A-sensor was closer to the sample edges and others using sensors representing H-coils (instead of Hall sensors) were carried out; however, the conclusions remained the same as the ones presented herein. A complimentary simulation using linear behavior showed that measurements at the surface for both locations were the same, confirming that, for linear isotropic materials, the UC is always met.

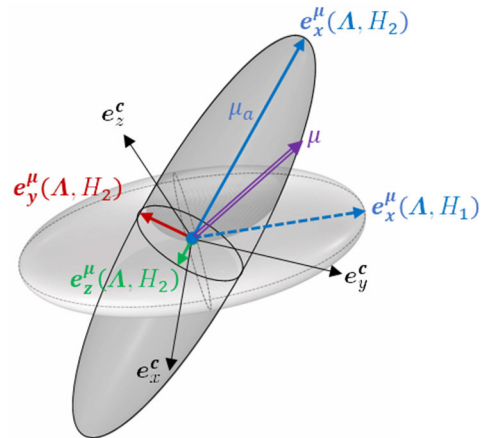


Fig. 4. Elliptic permeability μ . Light gray (resp. dark gray) ellipsoid corresponds to $H = H_1$ (resp. $H = H_2$). $R_c(e_x^c, e_y^c, e_z^c)$ (resp. $R_\mu(e_x^\mu, e_y^\mu, e_z^\mu)$) is the characterization (permeability) reference frame.

2) *Anisotropic Material*: Throughout this article, the permeability for anisotropic materials is chosen elliptic ($\mu = \text{diag}(\mu_a, \mu_b, \mu_c)$). Fig. 4 shows μ for two values of H magnitude (H_1 : light gray and H_2 : dark gray ellipsoids). Note that, for a linear behavior, there is only a single ellipsoid. The reference $R_\mu(e_x^\mu, e_y^\mu, e_z^\mu)$ is attached to μ -ellipsoid. For the sake of generality, both μ -ellipsoid shape (given by μ_a, μ_b , and μ_c) and orientation with respect to R_c can depend on H and other factors (denoted Λ) such as applied or residual stress.

Euler angles between R_c and R_μ are denoted by ϕ_1 , ψ , and ϕ_2 (around e_z^c , e_y^c , and e_x^c) and the direction cosines matrix (corresponding to the sequence $e_z^c \rightarrow e_y^c \rightarrow e_x^c$) by C .

Throughout this article, the dependence of ϕ_1 , ψ , and ϕ_2 on \mathbf{A} and H is described as follows: $\phi_1(\mathbf{A}, H) = \phi_1(\mathbf{A}) + \phi_1(H)$ (identical decomposition is done for ψ and ϕ_2). In this paragraph, R_μ is chosen to coincide with R_c (i.e., $\phi_1(\mathbf{A}) = \phi_1(H) = \psi(\mathbf{A}) = \psi(H) = \phi_2(H) = \phi_2(\mathbf{A}) = 0$). Four samples (Sx, Sy, Sz, and Sxz) are studied: the first cut along the e_x^c -direction, the second e_y^c , and the third e_z^c , and the fourth is cut in the (e_x^c, e_z^c) plane at 30° angle from e_z^c .

In this paragraph, the simulation is carried out a location A. It was found that, for the three samples cut along the principal permeability axes, \mathbf{B} & \mathbf{H} are collinear, and their direction—practically constant—is along the sample(s) length (e_z^S). As a result, all three principal permeabilities were obtained using $\mu_i = B_z^{Si} / \mu_0 H_z^{Si}$, where $i \in \{x, y, z\}$. These permeabilities were calculated from measurements at a single point, on the surface, and above the surface (using 1A sensor for \mathbf{H}); however, no significant discrepancies were found between them and the ones describing the real material behavior. As for the sample Sxy, the simulation showed that $B_x \approx B_y \approx 0$; however, \mathbf{B} & \mathbf{H} were not collinear, and the direction of \mathbf{H} changed significantly throughout the experiment. On the one hand, using S_{xz} can, in practice, be disadvantageous for characterization since 3-D measurements are needed. On the other hand, such a sample offers a way to measure simultaneously both μ_a and μ_c . To illustrate this, (1) is written in the sample reference frame as $\mathbf{B} = [C_{\mu \rightarrow Sxz} \cdot \boldsymbol{\mu} \cdot C_{\mu \rightarrow Sxz}^T] \cdot \mathbf{H}$, where $C_{\mu \rightarrow Sxz}$ is the direction cosines matrix mapping R_μ to R_{Sxz} . In the present case, R_{Sxz} is found by rotating R_μ around e_y^c by 30° angle. Upon doing the calculations, one finds

$$\mu_a = \frac{\sqrt{3}B_x + B_z}{\mu_0(\sqrt{3}H_x + H_z)} \quad (7a)$$

$$\mu_c = \frac{\sqrt{3}B_x - B_z}{\mu_0(\sqrt{3}H_x - H_z)}. \quad (7b)$$

Though it is possible to compute also μ_b , from the simulation results (since the out-of-plane components B_y and H_y are not exactly equal to zero in this example), in practice, small magnitudes are difficult to measure accurately. Fig. 5(a) gives the three principal permeabilities computed from samples Sx, Sy, and Sz (dot markers). Dashed (resp. dotted) lines give μ_a & μ_c computed from the sample Sxz for measurement made at the surface (resp. above the surface using 1A sensor for \mathbf{H}). The discrepancies between the two results stem from the fact that the fulfillment of BHmC varies from sample to sample. Here, for example, it is that of the CC since the difference between the \mathbf{H} field on the surface and above the surface is much larger for Sxz than the other samples (see Fig. 5(b), which gives the direction cosines as functions of the experiment time).

Complementary cases were studied: in the first, the disparity between the principal permeabilities was more pronounced; in the second, the sample width was 80 mm (instead of 20 mm); and in the third, the μ -ellipsoid direction was dependent on

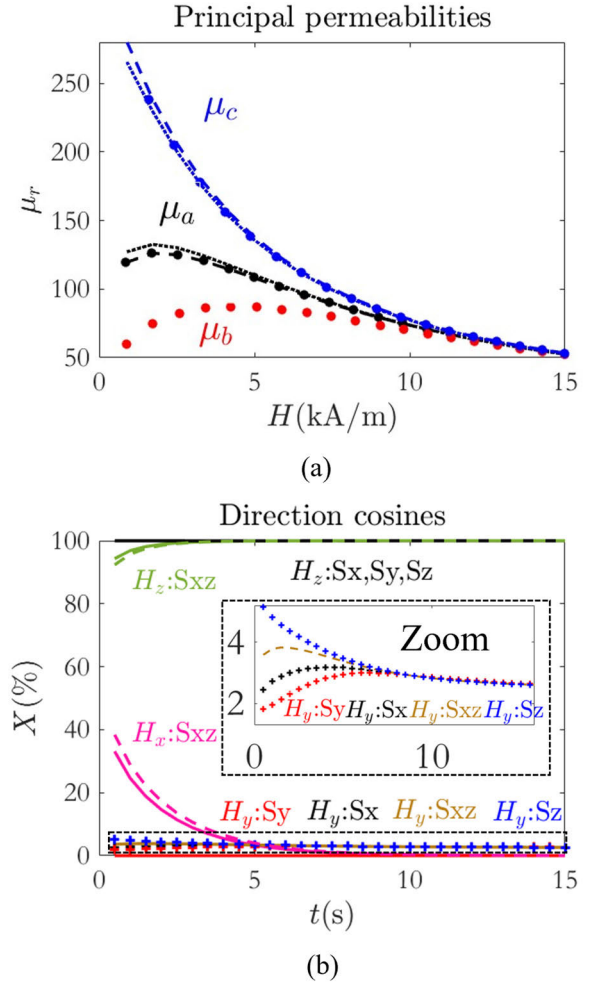


Fig. 5. (a) Dot makers give the principal permeabilities computed from measurements carried out using the samples Sx, Sy, and Sz (i.e., samples cut along the principal permeability axes). Dashed (resp. dotted) lines give μ_a & μ_c computed from measurements carried out at the Sxz surface (resp. above the surface). (b) Direction cosines of \mathbf{H} for all samples: those of Sx, Sy, and Sz at the surface (not shown for lack of space) are practically the same as the ones above the surface. Red (resp. black) line corresponds to $H_x : Sx, Sy, Sz$ (resp. $H_z : Sx, Sy, Sz$). Solid green, pink, and brown (resp. dashed) lines correspond to Sxz at the surface (resp. above the surface).

the norm of the field. All cases showed that, in general, \mathbf{B} is not always along the sample length. To overcome such an issue, in practice, the search coil wound around the sample should be replaced by a sensor that allows measuring at least two components (e.g., B-needles). In conclusion, this paragraph showed that, in addition to the sample geometry and measurement location, the orientation of the cut sample also affects the fulfillment of the measurement criteria. In practice, for this particular apparatus, narrower samples are better, and in general, \mathbf{H} should be measured as close to the surface as possible.

B. 2-D Systems

The characterization of a nonlinear anisotropic material (with unknown anisotropy) requires full mapping of both the field magnitude (from low to saturation) and direction (in 3-D space). Though such mapping can be carried out randomly, applications from the literature follow two

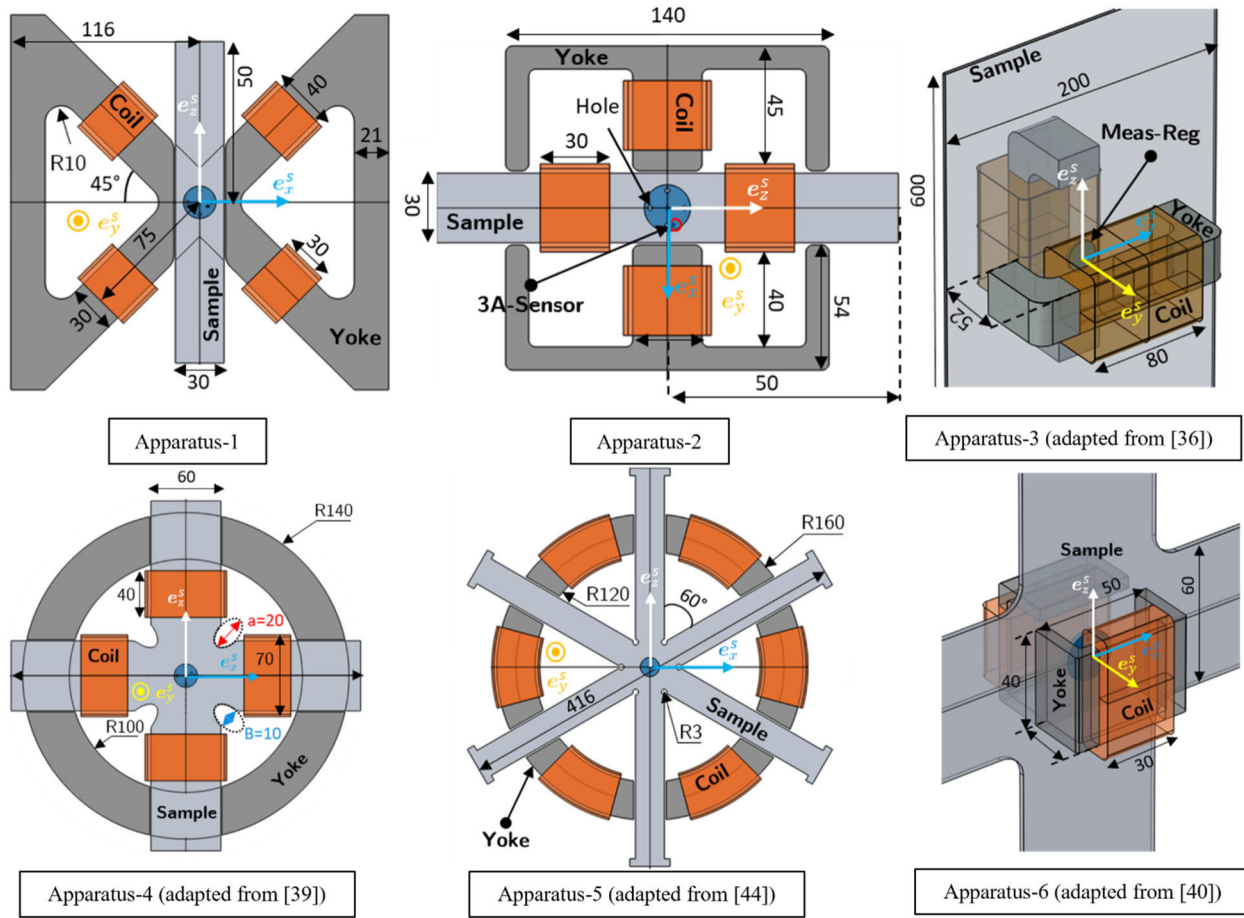


Fig. 6. Six studied apparatuses. The blue area is the B measurement region (i.e., a cylinder of height 2 mm—equal to the sample thickness—and radius 10 mm), and the position of the 3A-sensor (R_H origin: $x = 6.5$ mm, $y = 2.5$ mm, and $z = 2.5$ mm) of the 3A-sensor is the same for all apparatuses. The holes of 1 mm radius are 15 mm apart (see apparatus-2). The first three apparatuses allow the application of only uniaxial stress, and the other three allow the application of both uniaxial and biaxial in-plane stress. The origin of the sample reference frame R_s coincides with the center of the B measurement region. R_s and R_B (the reference frame attached to the B-sensor) are chosen to coincide. (Dimensions are in mm.)

“ordered” approaches (loadings): fixing the direction and varying the magnitude (alternating) or fixing the magnitude and varying the direction (rotating). Only 2-D excitation systems allow for the implementation of the second approach. The fulfillment of BHmC is studied for both isotropic and anisotropic materials. While characterizing anhysteretic isotropic materials does not require the use of a 2-D system, such materials enable assessment of the “unwanted” change of direction (resp. magnitude) in the alternating (resp. rotating) approach. Aside from allowing for gauging the misorientation between B & H sensors, isotropic materials also help isolate and study the effect of nonlinearity in the rotating approach. While many apparatuses were studied (more than 20), only six are presented here (see Fig. 6). Apparatuses 1 and 2 are new proposals, while the other four are chosen to represent the ones commonly used in the literature. Three of the six allow the application of only uniaxial stress, and the other three allow the application of both uniaxial and biaxial stress. A 1-mm air gap is left between the yoke(s) and the sample for all apparatuses in this article.

The reasons for the choice of these apparatuses are given as follows: apparatus-1 has all coils on the same material (i.e., the yokes) in contrast to apparatus-2, where two coils are

on the sample, and the other two are on the yokes. Apparatus-3 gives freedom on the yoke orientations and allows having them manually rotated (like the one in [36]). The sample shape in apparatus-4 was inspired by one of the samples in [39]. Apparatus-5 is very close to the one in [44], and apparatus-6 can be considered as the biaxial version of apparatus-3. All samples have a center of symmetry, which coincides with the origin of the sample reference frame R_s . In all apparatuses, the B measurement region (a cylinder of height 2 mm—equal to the sample thickness—and radius 10 mm) and the position of the 3A-sensor (R_H origin: $x = 6.5$ mm, $y = 2.5$ mm, and $z = 2.5$ mm, coordinates taken with respect to R_s) are the same. As in Section III-A, R_s and R_B (the reference frame attached to the B-sensor) are chosen to coincide. Other studies wherein the 3A-sensor position was different (R_H origin: $x = 0$ mm, $y = 2.5$ mm, and $z = 0$ mm) were also carried out. Though their results may differ from the ones presented here, the drawn conclusions remain the same.

1) *Isotropic Materials:* The $B(H)$ curve is the same throughout this section [dot markers in Fig. 7(a)]. Results for the six apparatuses (numbered 1–6) are given in the Appendix. For each apparatus, alternating (Alt) and rotating (Rot) field

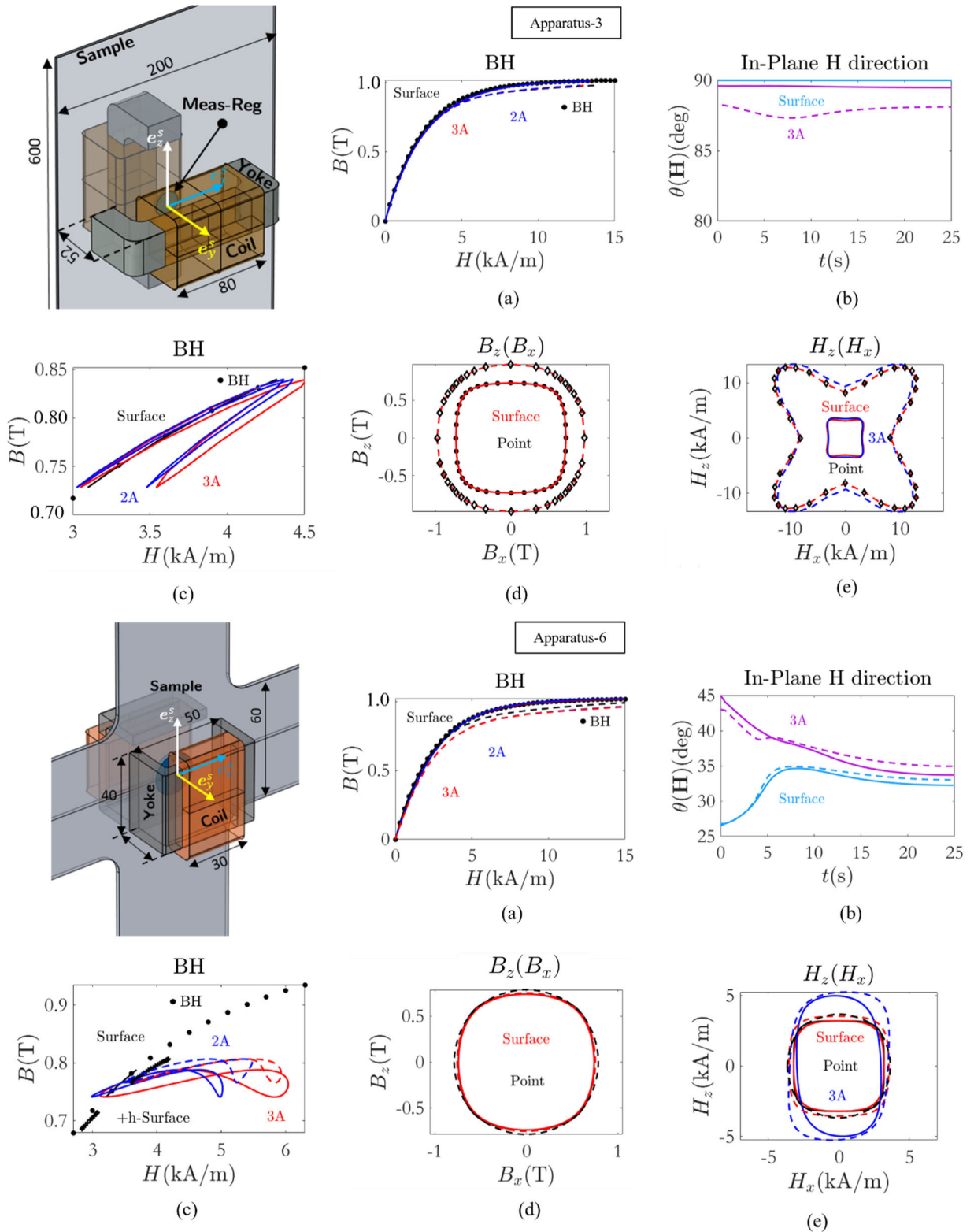


Fig. 7. (a) Alternating results (seven curves): dot markers give the real material behavior, and solid (resp. dashed) lines give the measurement without (rep with) holes in the B measurement region. Measurements carried out at the surface are given in black, those using 3A-sensor, in red, and those using 2A-sensor in blue. (b) Alternating results (four curves): the in-plane H field direction on the surface and at the 3A-sensor location. (c)–(e) Rotating results: for apparatus-3, they correspond to midfield magnitude (solid lines) and close to saturation (dashed and diamond markers); for apparatus-6, they correspond to the case without holes in the B measurement region (solid lines) and with holes (dashed lines).

loadings are studied, and 26 measurements are presented. These are summarized in Table III.

Each measurement is carried out with and without drilled holes in the B measurement region (the holes' radii equal

1 mm and are 15 mm apart). The results of the two apparatuses that fulfill the BHmC the most (i.e., 3 and 6) are given in Fig. 7. Fig. 7(a) and (b) corresponds to the alternating approach, and those of the rotating approach are in

TABLE III

MEASUREMENTS CARRIED OUT FOR EACH APPARATUS. THE FIRST COLUMN GIVES THE TYPE OF MEASUREMENT (\mathbf{H} DIRECTION AND IN-PLANE \mathbf{H} DIRECTION ARE GIVEN AS FUNCTIONS OF THE EXPERIMENT TIME). THE SECOND COLUMN GIVES THE LOCATION OF THE MEASUREMENT, AND THE FOURTH GIVES THE NATURE OF THE APPROACH (ALTERNATING OR ROTATING)

Measurement	Location	Alt/Rot
$B(H)$	Point	Alt & Rot
	Surface	Alt & Rot
	Above surface ($H_{out} = 0$)	Alt & Rot
	Above surface ($H_{out} \neq 0$)	Alt & Rot
\mathbf{H} direction	Surface	Alt & Rot
	Above surface	Alt & Rot
In-plane \mathbf{H} direction	Surface	Alt & Rot
	Above surface	Alt & Rot
$H_z(H_x)$	Point	Rot
	Surface	Rot
	Above surface	Rot
$B_z(B_x)$	Surface	Rot
	Above surface	Rot

Fig. 7(c)–(e). Dot markers in Fig. 7(a) give the real $B(H)$ curve, and solid (resp. dashed) lines give the results without (resp. with) holes. Measurements at the sample surface (assuming the out-of-plane field components B_y & H_y null) are in black, those above the surface using 3A-sensor (not assuming $H_y = 0$) are in red, and those assuming $H_y = 0$ are in blue. The measurement at the surface coincides with the real material behavior (this is true for all apparatuses), which implies that both uniformity and direction criteria are respected. The discrepancies emerging when \mathbf{H} is no longer measured at the surface (3A and 2A) are the result of an ill-respected CC (for 3A and 2A) and DC (for 2A).

For all results, the presence of holes (represented by simply the absence of matter in the simulation) degrades the accuracy. It is worth emphasizing that, in practice, drilling a hole does not simply mean taking some matter out but also modifying stress distribution and material properties in its vicinity. Results in the Appendix show that the out-of-plane component on the surface is null for all apparatuses; however, it can become large ($100H_{out}/H \approx 60\%$) at 1 mm from the surface for apparatuses 1 and 2. This shows that the assumption that, in 2-D systems, the fields are mostly in-plane near the surface is not always valid. Fig. 7(b) gives the in-plane field direction for the alternating loading conditions. Though currents in each direction are imposed [e.g., for apparatus-6: $I_{ex}(t) = 2I_0 \sin(0.02t\pi) = 2I_{ez}(t)$ and for apparatus-3, $I_{ex}(t) = 0$ and $I_{ez}(t) = 2I_0 \sin(0.02t\pi)$], the field still changes direction throughout the experiment time. An auxiliary simulation, wherein $B(H)$ is linear, showed that this effect is due to the nonlinearity. In essence, since the material does not get magnetized uniformly, some parts will have higher permeability; as a result, they attract the field from the parts with lower permeability, thereby changing the field direction. Fig. 7(b) shows that the change is more

pronounced for apparatus-6 than 3. This is because yokes were mirror images of each other for apparatus-3 and at a right angle for 6. Fig. 7(c) and (d) gives the results for the rotating approach. The rotating magnetic field is obtained by imposing sinusoidal currents with 90° phases (three-phase currents for apparatus-5 in the Appendix). Apparatus-3 was chosen to compare results at midfield magnitude [solid lines in Fig. 7(c)–(e)] and close to saturation [dashed lines and diamond markers in Fig. 7(d) and (e)]. Results in Fig. 7(c) show that measurements at the surface without holes (solid black lines) are the most accurate—those above the surface yield loops (more pronounced for apparatus-6). The loops stem from the fact that the magnetic field at the surface (collinear with \mathbf{B}) is noncollinear with that above the surface.

Aside from the noncollinearity, such loops can result from misalignment between \mathbf{B} & \mathbf{H} sensors (this was shown in a separate simulation). The fact that, once again, the 2A-sensor results are closer to the real material behavior than those of the 3A-sensor is merely due to two errors compensating each other. The first is that the sensor is closer to the coils; as a result, \mathbf{H} at the sensor location is larger than the one at the surface (giving rise to the measured \mathbf{B}). This correspondence error is compensated by the second error introduced by—only—the 2A-sensor since it measures the projection of the field (multiplying the norm by a cosine < 1). Fig. 7(d) and (e) gives $B_z(B_x)$ [resp. $H_z(H_x)$]. Note how imposing a circular current does not necessarily yield circular \mathbf{H} or \mathbf{B} . Results of the rotating approach ($B_z(B_x)$ and $H_z(H_x)$) are functions of the excitation system, the sample material, and geometry. The fact that $H_z(H_x)$ is different from $B_z(B_x)$ is a result of the nonlinear behavior. This was shown in a complementary study using linear materials. While results for the six apparatuses may vary from each other, the conclusions remain the same.

- 1) The assumption that the fields are in the plane near the surface is not always valid (error = $[100H_{out}/H]$ can reach 80%; see apparatus-2 in the Appendix). The DC is, thus, respected by measuring all three vectorial components.
- 2) Holes drilled in the sample reduce the fulfillment of the UC, thereby degrading the measurement accuracy.
- 3) Since \mathbf{H} at 1 mm above the surface differs—from that at the surface (error $\approx 40\%$ for apparatus-6), the fulfillment of the CC can be improved by moving the sensor closer to the surface.
- 4) When currents are imposed, the fields can change direction (resp. magnitude) in alternating (resp. rotating) approaches.

The change of magnitude in the rotating loading was eliminated in a separate simulation, wherein the yokes in apparatus-3 were set to mirror images of each other and were rotated (instead of imposing circular current). They also can be eliminated if \mathbf{B} or \mathbf{H} is imposed.

2) *Anisotropic Materials*: Apparatus-6 is chosen to assess the fulfillment of BHmC in the case of anisotropic materials. In the present case, anisotropy is not inherent to the material (like the one studied in Section II-A) but rather induced by applied mechanical stress. The analytical version of the

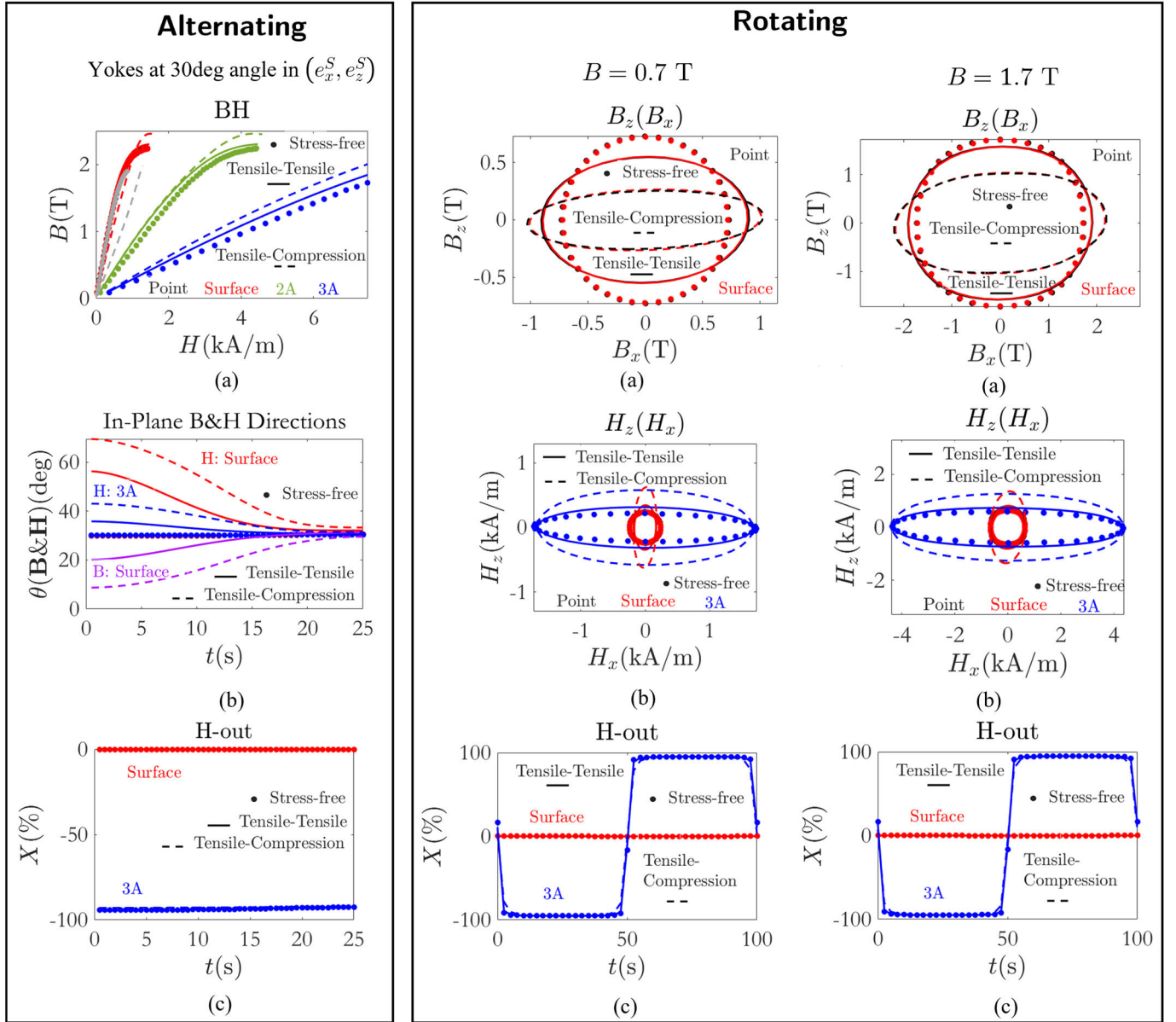


Fig. 8. Results for apparatus-6. Dot markers correspond to the stress-free case. Continuous solid (resp. dashed) lines correspond to $\{\sigma_x = 10 \text{ MPa}$ and $\sigma_z = 20 \text{ MPa}\}$ (resp. $\{\sigma_x = 10 \text{ MPa}$ and $\sigma_z = -20 \text{ MPa}\}$). Black (resp. red) color is used for measurements at a single point (resp. surface), and blue color is used when the \mathbf{H} field is measured using the 3A-sensor above the surface. Alternating: in (a), green is used for when H_{out} is assumed null, and gray is used for when holes are present in \mathbf{B} measurement region. (b) In-plane fields directions as functions of time and (c) the out-of-plane magnetic field component. Rotating: (a) (resp (b)) the z -component as a function of the y -component of the magnetic induction (resp magnetic field) and (c) the out-of-plane components.

multiscale model [46] is used to model the effect of applied multiaxial stress on an isotropic material. Such a model gives the permeability in the direction of the applied magnetic field under applied multiaxial stress (see [46])

$$\mu_i = 1 + \frac{A_i \sinh(\kappa H)}{A_i \cosh(\kappa H) + \sum_j A_{j \neq i}} \frac{M_s}{H} \quad (8)$$

where M_s is the saturation magnetization; $\kappa = \mu_0 A_s M_s$ (where $A_s = 3\chi_0/\mu_0 M_s^2$ and χ_0 is the initial susceptibility of the anhysteretic curve under no applied stress); and $A_i = \exp(\alpha \sigma_i)$, $i \in \{x, y, z\}$, where $\alpha = (3/2)A_s \lambda_s$ (λ_s is the maximum magnetostriction strain). The numerical values of the parameters for the present case are given as follows: $M_s = 1.810^6 \text{ A/m}$, $\kappa = 4 \times 10^{-3} \text{ m/A}$, and $\alpha = 10^{-7} \text{ Pa}^{-1}$.

Due to the high material permeability, the yoke permeability was set at 80000 (instead of 10000 used thus far).

Fig. 8 shows the results for alternating (first column) and rotating (second and third column) loadings. Dot markers correspond to the stress-free case, for which the material is isotropic. Continuous solid lines correspond to applied in-plane biaxial tensile stress ($\sigma_x = 10 \text{ MPa}$ and $\sigma_z = 20 \text{ MPa}$). Dashed lines correspond to $\sigma_x = 10 \text{ MPa}$ and $\sigma_z = -20 \text{ MPa}$. Black (resp. red) color is used for measurement at a single point (resp. surface), and blue color is used when the \mathbf{H} field is measured using the 3A-sensor above the surface. Measurements for the alternating approach are carried out when the yokes (mirror images of each other) are at a 30° angle from e_x^S (in the (e_x^S, e_z^S) plane). Other studies with the yokes

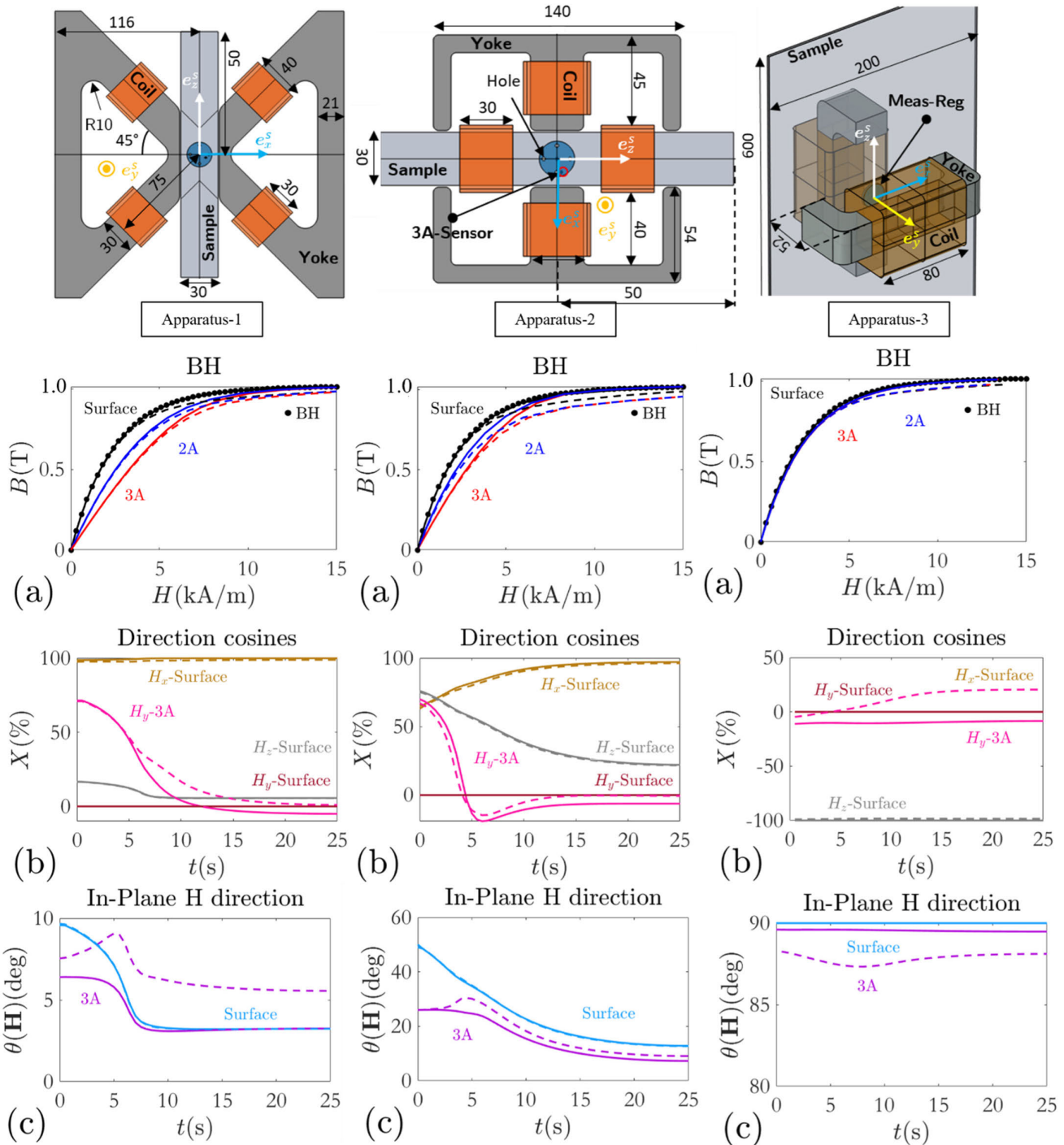


Fig. 9. Alternating results. All dimensions are in mm: apparatuses allowing for the application of only uniaxial stress. (a) Seven curves: dot markers give the real material behavior ($B(H)$), and solid (resp. dashed) lines correspond to the case when there are no holes in the B measurement region (resp. when there are). Measurements carried out at the surface (for both B & H) are given in black, and those using 3A-sensor (resp. 2A-sensor) for H , while B is measured at the surface, are in red (resp. blue). (b) Direction cosines of H (i.e., $X = 100H_i/H$) at the surface and the out-of-plane component (H_y) above the surface (at 1 mm, i.e., at the 3A-sensor location) with (dashed lines) and without holes (solid lines). (c) Four curves: the in-plane H field direction ($\theta = \text{atan}(H_z/H_x)$) at the surface and at the 3A-sensor location, as a function of the experiment time with (dashed lines) and without holes (solid lines).

at 0° , 45° , and 60° were also carried out; the conclusions, however, remain the same. For this loading, Fig. 8(a) gives $B = f(H)$. Measurements at a single point and on the surface coincide, which implies that the UC is respected. Measurements above the surface (green corresponds to when assuming $H_{\text{out}} = H_y = 0$) are significantly different from those at the surface. This stems from an ill-respected CC.

Gray curves in Fig. 8(a) represent measurements carried out at the sample surface when holes are present. Note how the deviation between the stress-free and under-stress cases is the largest for such a case. The reason is that magnetic field and mechanical stress are concentrated around holes. As a result, the magnetomechanical coupling amplifies the error due to nonuniformity. The effect of stress on the fulfillment of BHmC

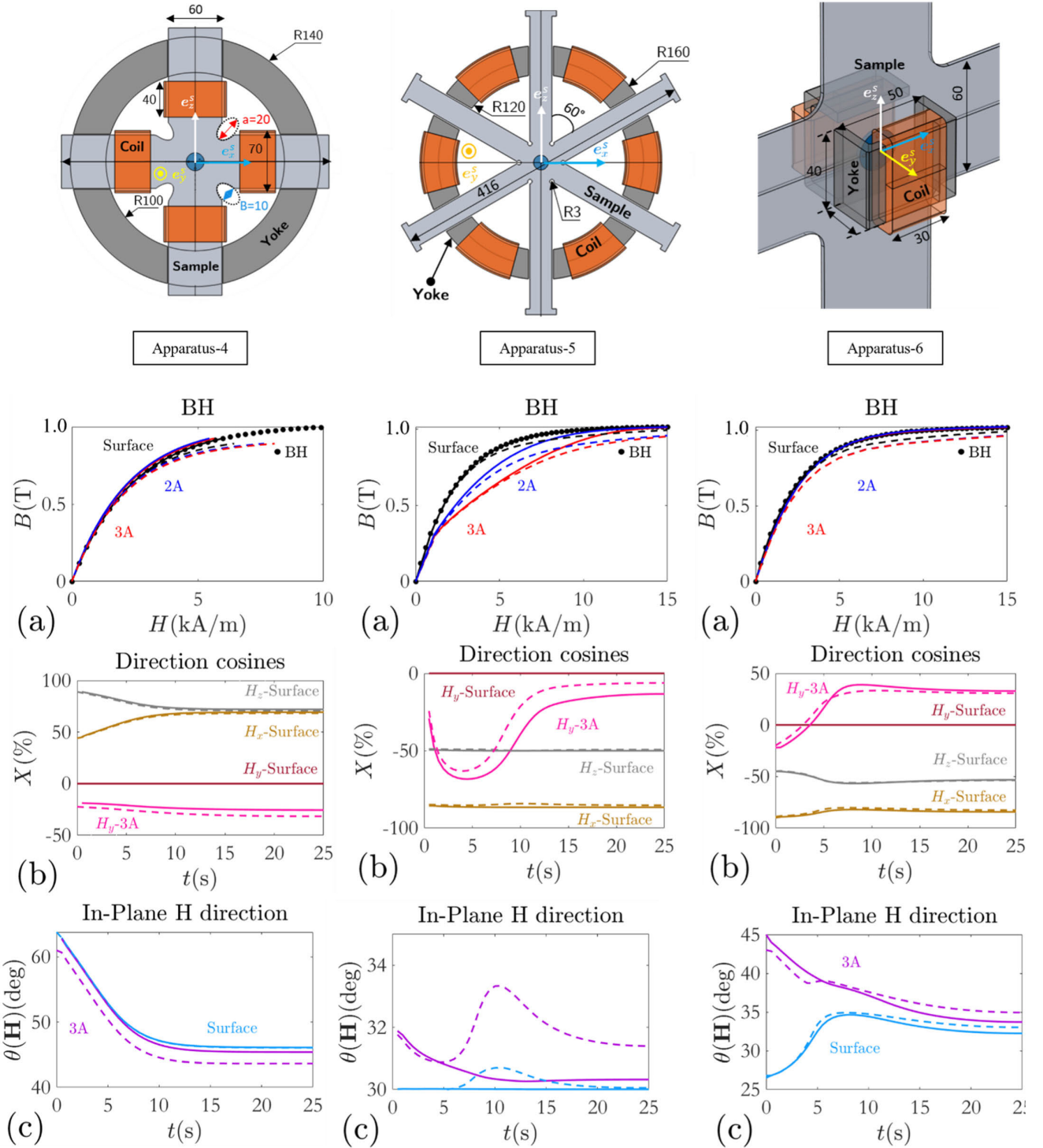


Fig. 10. Alternating results. All dimensions are in mm: apparatuses allowing for the application of both uniaxial and biaxial stress. (a) Seven curves: dot markers give the real material behavior ($B(H)$), and solid (resp. dashed) lines correspond to the case when there are no holes in the B measurement region (resp. when there are). Measurements carried out at the surface (for both B & H) are given in black, and those using 3A-sensor (resp. 2A-sensor) for H , while B is measured at the surface, are in red (resp. blue). (b) Direction cosines of H (i.e., $X = 100H_i/H$) at the surface and the out-of-plane component (H_y) above the surface (at 1 mm, i.e., at the 3A-sensor location) with (dashed lines) and without holes (solid lines). (c) Four curves: the in-plane H field direction ($\theta = \text{atan}(H_z/H_x)$) at the surface and at the 3A-sensor location, as a function of the experiment time with (dashed lines) and without holes (solid lines).

is more noticeable in Fig. 8(b), wherein the in-plane directions ($\text{atan}(H_z/H_x)$ and $\text{atan}(B_z/B_x)$) as functions of the experiment time are presented. For the stress-free case, the fields remain at 30° throughout the experiment (i.e., the direction set by the yokes), both at the surface and above the surface. When stress is applied, B & H are no longer collinear and are not

in the yokes direction. Their directions change over time and depend on stress. Fig. 8(c) shows that, with and without stress, H above the surface (at 1 mm) is almost ($X(H_{\text{out}}) \approx 95\%$) normal to the surface.

The results for the rotating loading at $B \approx 0.7$ T (resp. 1.7 T) are given in the second (resp. third) column of Fig. 8.

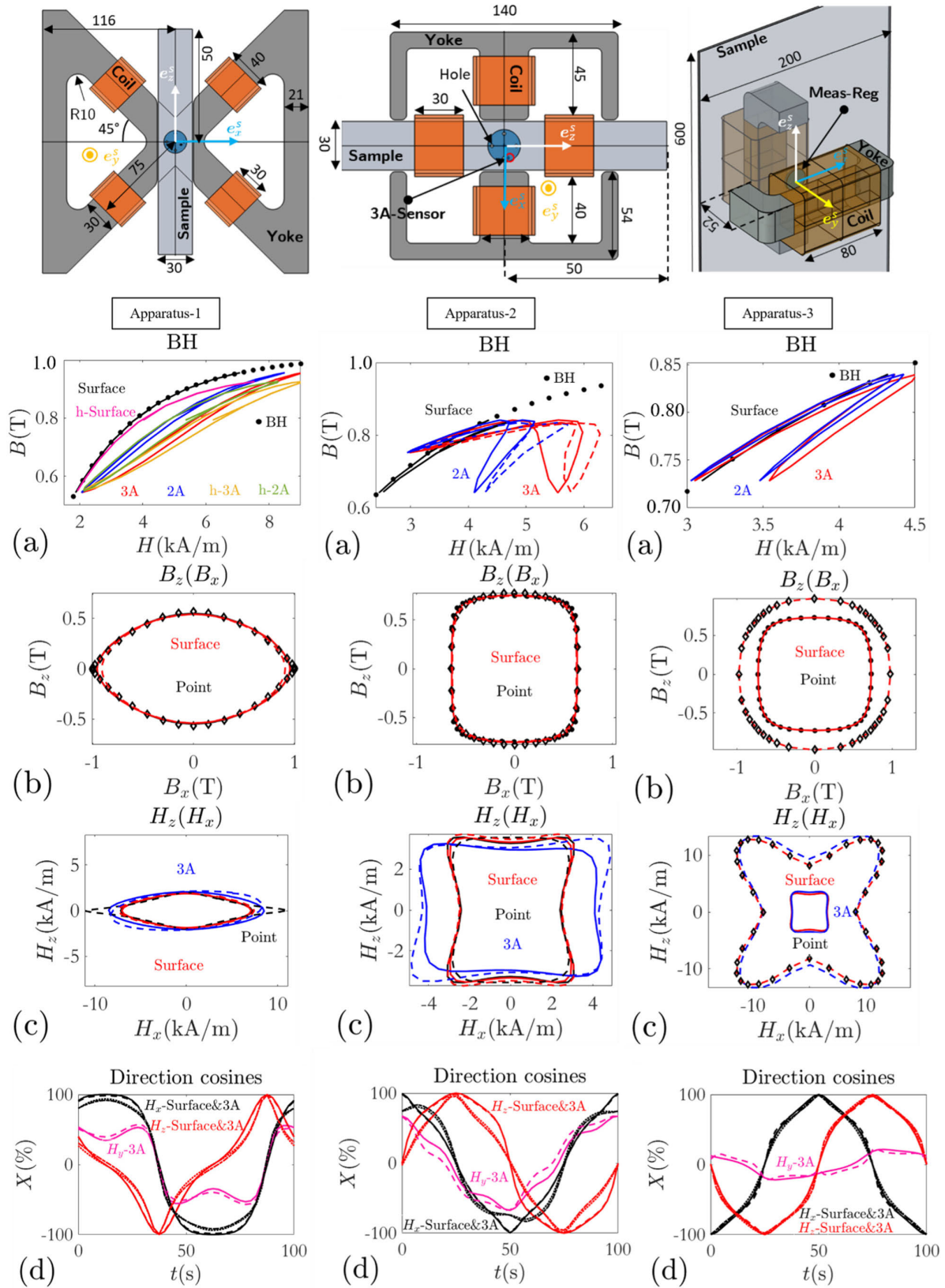


Fig. 11. Rotating results. All dimensions are in mm: apparatuses allowing for the application of only uniaxial stress. (a) Dot markers give the real material behavior ($B(H)$). For apparatus-1 (resp. apparatus-2), the presence of holes is indicated by using "h" in the legend (resp. dashed lines). For apparatus-3, measurements are carried out without holes. (b) For apparatus-1 and apparatus-2, dashed and diamond markers give measurements with holes; for apparatus-3, they give measurements close to saturation ($B \approx 1$ T). (c) $H_z(H_x)$ at a point in the material (black), at the surface (red), and at the 3A-sensor location (blue). (d) Ten curves: direction cosines ($X = 100H_i/H$) of the H field at the surface and the 3A-sensor location. Dashed (resp. solid) lines represent apparatus-1 and apparatus-2, the case with holes (resp. without holes), and apparatus-3 midfield magnitude (resp. close to saturation).

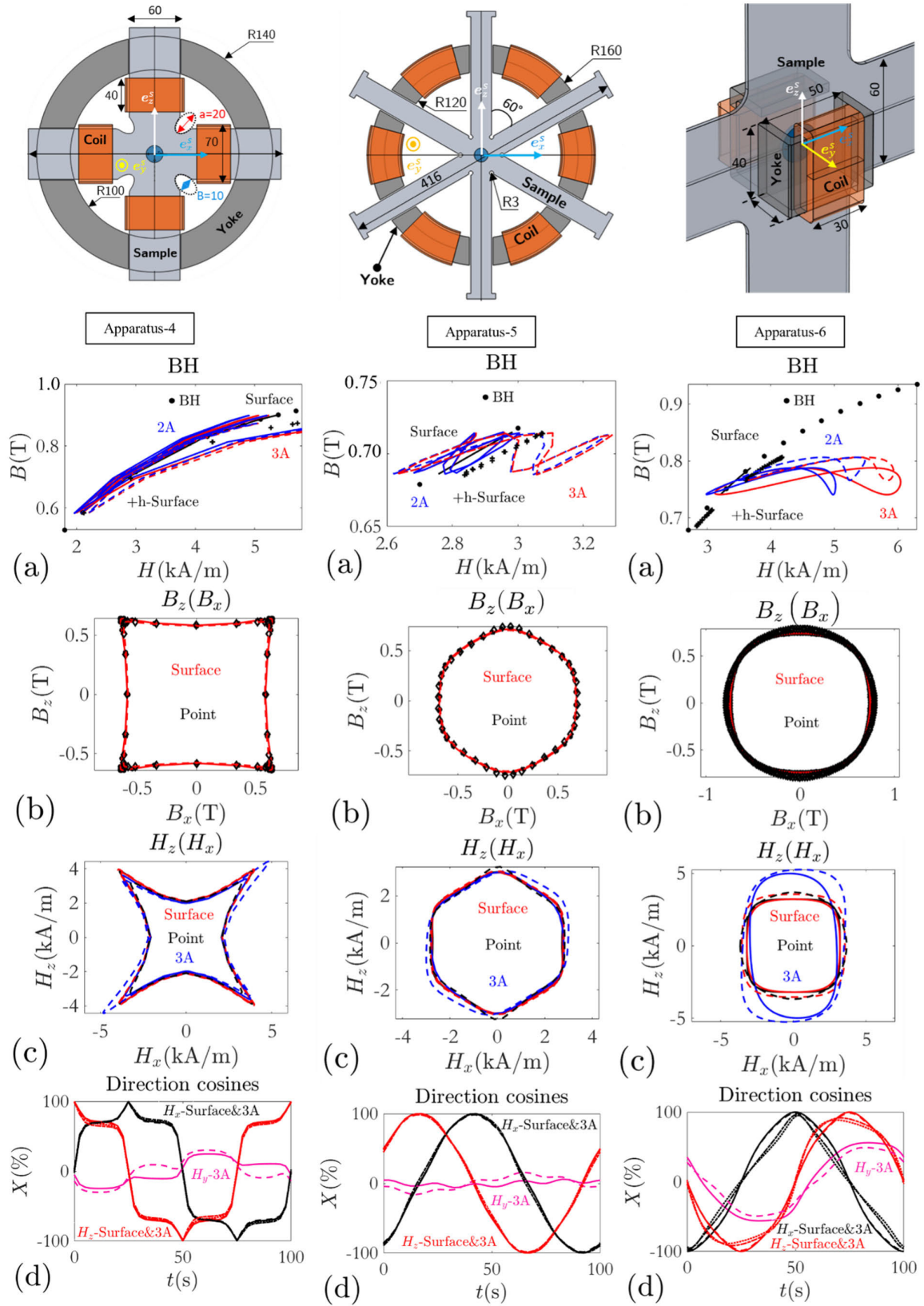


Fig. 12. Rotating results. All dimensions are in mm: apparatuses allowing for the application of both uniaxial and biaxial stress. (a) Dot markers give the real material behavior, and solid (resp. dashed and “+” markers) lines give the measurements when there are no holes in the \mathbf{B} measurement region (resp. when there are). (b) $B_z(B_x)$ at a single point and on the surface for when there are holes (dashed lines and diamond markers) and when there are not (solid lines). (c) $H_z(H_x)$ at a point in the material (black), at the surface (red), and at the 3A-sensor location (blue). (d) Ten curves: direction cosines ($X = 100H_i/H$) of the \mathbf{H} field at the surface and the 3A-sensor location. Dashed (resp. solid) lines represent apparatus-1 and apparatus-2, the case with holes (resp. without holes), and for apparatus-3 midfield magnitude (resp. close to saturation).

Conclusions drawn from the alternating loading also apply here.

- 1) Measurements at a single point and on the surface coincide (well-respected UC).
- 2) Those above the surface are significantly different (ill-respected CC).
- 3) The magnetic field at 1 mm from the surface is almost normal to the surface.

IV. CONCLUSION

This work dealt with the question of the magnetic characterization of magnetic materials. It puts forth three criteria that form a condition that is both necessary and sufficient for reliable measurements. These criteria are derived from the underlying assumptions made in every magnetic characterization experiment, which are usually not explicitly established nor verified.

- 1) The material magnetic properties are assumed homogeneous in the measurement region (UC).
- 2) The measured magnetic field \mathbf{H} is equal to the one giving rise to the measured magnetic induction \mathbf{B} (CC).
- 3) \mathbf{B} & \mathbf{H} directions are known throughout the experiment time (DC).

The criteria are indicators of how much these assumptions are respected for a given apparatus. The necessity and sufficiency of the criteria were first proven theoretically. Simulations were then used to assess their fulfillment for various apparatuses. Both alternating and rotating approaches were considered for linear and nonlinear behaviors, using isotropic and anisotropic materials in both 1-D and 2-D excitation and measurement systems, with and without applied mechanical stress. The main conclusions of this work are given as follows.

- 1) When all three criteria are well-respected, measurements yield the material behavior.
- 2) Apparatuses with ill-respected criteria can yield constitutive relations that are significantly (an order of magnitude) different from the real ones.
- 3) Errors from ill-respected criteria can be added to or subtracted from each other.
- 4) UC is always well-respected for isotropic materials exhibiting linear behavior. For anisotropic and/or nonlinear behavior, its fulfillment depends on material properties.
- 5) Improving UC fulfillment can be achieved by decreasing the measurement region size and lowering the excitation frequency to avoid through-thickness nonuniformity due to eddy currents.
- 6) Drilled holes (to wound B-coils) introduce geometric inhomogeneity, thereby hindering UC fulfillment.
- 7) CC is always respected if \mathbf{B} & \mathbf{H} measurement regions coincide (e.g., \mathbf{B} & \mathbf{H} measurements are carried out at the sample surface).
- 8) \mathbf{H} at 1 mm from the surface can significantly differ—in both magnitude and direction—from the one at the surface.
- 9) Misorientations between \mathbf{B} & \mathbf{H} sensors can be reduced using isotropic materials.

- 10) \mathbf{B} & \mathbf{H} directions should be known throughout the experiment time (DC).
- 11) The fulfillment of the criteria can vary greatly from material to material and apparatus to apparatus.
- 12) Apparatuses for which the \mathbf{B} & \mathbf{H} measurements regions are far apart or using the magnetic path length method can hardly fulfill the measurement criteria and, if possible, should be avoided.

In summary, the conclusions presented herein point toward two recommendations that are independent of apparatus and material properties: 1) measurements should be carried out in 3-D space (B_{out} can be measured using the continuity of the normal magnetic induction component boundary condition) and 2) if possible, both \mathbf{B} & \mathbf{H} should be measured at the surface (in this case, through-thickness uniformity is not required, which allows an increase in the frequency, though resulting dynamic effects should be considered). If not, \mathbf{H} should be measured as close to the sample surface as possible. Finally, while simulations were carried out using anhysteretic behavior, and only a few sensor types were considered (i.e., Hall sensor, H-coil, and B-coil), the conclusions presented herein remain the same for hysteresis and other types of sensors. This is because the measurement criteria are time-independent and, therefore, also apply to hysteretic behavior. Furthermore, active areas of sensors can be represented by points, surfaces, or volumes, which were all considered in this work. It was also shown that, in most cases, the criteria are satisfactorily fulfilled by 1-D excitation systems. 2-D systems offer more refined information (the ability to allow rotating fields and multiaxial loading), but they are prone to more significant measurement errors. Finally, this work shows the utmost importance of simulating the experimental setups before measurements to support the design and after measurements to quantitatively identify the uncertainty sources.

APPENDIX

See Figs. 9–12.

REFERENCES

- [1] R. M. Bozorth, *Ferromagnetism*. New York, NY, USA: Van Nostrand Company, 1951, pp. 595–712.
- [2] B. D. Cullity and C. D. Graham, *Introduction to Magnetic Materials*. Hoboken, NJ, USA: Wiley, 2011, pp. 241–273.
- [3] D. C. Jiles and D. L. Atherton, “Theory of the magnetisation process in ferromagnets and its application to the magnetomechanical effect,” *J. Phys. D, App. Phys.*, vol. 17, no. 6, p. 1265, 1984.
- [4] D. C. Jiles, “Theory of the magnetomechanical effect,” *J. Phys. D, App. Phys.*, vol. 28, p. 1537, Aug. 1995.
- [5] L. Daniel, M. Rekik, and O. Hubert, “A multiscale model for magnetoelastic behaviour including hysteresis effects,” *Arch. Appl. Mech.*, vol. 84, nos. 9–11, pp. 1307–1323, Oct. 2014.
- [6] L. Bernard and L. Daniel, “Effect of stress on magnetic hysteresis losses in a switched reluctance motor: Application to stator and rotor shrink fitting,” *IEEE Trans. Magn.*, vol. 51, no. 9, pp. 1–13, Sep. 2015.
- [7] M. J. Sablik, H. Kwun, G. L. Burkhardt, and D. C. Jiles, “Model for the effect of tensile and compressive stress on ferromagnetic hysteresis,” *J. Appl. Phys.*, vol. 61, no. 8, pp. 3799–3801, Apr. 1987.
- [8] J. Sievert, “Recent advances in the one- and two-dimensional magnetic measurement technique for electrical sheet steel,” *IEEE Trans. Magn.*, vol. 26, no. 5, pp. 2553–2558, Sep. 1990.
- [9] T. Nakata, N. Takahashi, Y. Kawase, M. Nakano, M. Miura, and J. Sievert, “Numerical analysis and experimental study of the error of magnetic field strength measurements with single sheet testers,” *IEEE Trans. Magn.*, vol. MAG-22, no. 5, pp. 400–402, Sep. 1986.

- [10] M. Enokizono, T. Suzuki, J. Sievert, and J. Xu, "Rotational power loss of silicon steel sheet," *IEEE Trans. Magn.*, vol. 26, no. 5, pp. 2562–2564, Sep. 1990.
- [11] S. Zurek and T. Meydan, "Errors in the power loss measured in clockwise and anticlockwise rotational magnetisation. Part 1: Mathematical study," *IEE Proc.-Sci., Meas. Technol.*, vol. 153, no. 4, pp. 147–151, Jul. 2006.
- [12] S. Zurek and T. Meydan, "Rotational power losses and vector loci under controlled high flux density and magnetic field in electrical steel sheets," *IEEE Trans. Magn.*, vol. 42, no. 10, pp. 2815–2817, Oct. 2006.
- [13] N. Stranges and R. D. Findlay, "Measurement of rotational iron losses in electrical sheet," *IEEE Trans. Magn.*, vol. 36, no. 5, pp. 3457–3459, Sep. 2000.
- [14] W. Brix, K. Hempel, and W. Schroeder, "Method for the measurement of rotational power loss and related properties in electrical steel sheets," *IEEE Trans. Magn.*, vol. MAG-18, no. 6, pp. 1469–1471, Nov. 1982.
- [15] H. Geirinhas Ramos and P. Silva Girão, "A rotating field automated measurement system for the characterization of ferromagnetic materials," *J. Appl. Phys.*, vol. 69, no. 8, pp. 5103–5105, Apr. 1991.
- [16] K. Mori, S. Yanase, Y. Okazaki, and S. Hashi, "2-D magnetic rotational loss of electrical steel at high magnetic flux density," *IEEE Trans. Magn.*, vol. 41, no. 10, pp. 3310–3312, Oct. 2005.
- [17] A. Ivanyi, J. Fuzi, and H. Pftzner, "2D/3D models for a three phase fed single sheet tester," *IEEE Trans. Magn.*, vol. 34, no. 5, pp. 3004–3007, Sep. 1998.
- [18] M. Enokizono, I. Tanabe, and T. Kubota, "Localized distribution of two-dimensional magnetic properties and magnetic domain observation," *J. Magn. Magn. Mater.*, vol. 196, pp. 338–340, May 1999.
- [19] J. W. Wilson, N. Karimian, J. Liu, W. Yin, C. L. Davis, and A. J. Peyton, "Measurement of the magnetic properties of P9 and T22 steel taken from service in power station," *J. Magn. Magn. Mater.*, vol. 360, pp. 52–58, Jun. 2014.
- [20] S. Yue, A. J. Moses, P. I. Anderson, C. Harrison, Y. Li, and Q. Yang, "Measurement and analysis of the non-symmetry of transverse magnetisation and resulting loss in grain-oriented steel using a modified RSST," *J. Magn. Magn. Mater.*, vol. 561, Nov. 2022, Art. no. 169671.
- [21] S. H. N. Kouakeuo et al., "Internal characterization of magnetic cores, comparison to finite element simulations: A route for dimensioning and condition monitoring," *IEEE Trans. Instrum. Meas.*, vol. 71, pp. 1–10, 2022.
- [22] Y. Guo et al., "Measurement and modeling of magnetic materials under 3D vectorial magnetization for electrical machine design and analysis," *Energies*, vol. 16, no. 1, p. 417, Dec. 2023.
- [23] H. Kwun and G. L. Burkhardt, "Effects of grain size, hardness, and stress on the magnetic hysteresis loops of ferromagnetic steels," *J. Appl. Phys.*, vol. 61, no. 4, pp. 1576–1579, Feb. 1987.
- [24] O. Hubert and L. Daniel, "Multiscale modeling of the magneto-mechanical behavior of grain-oriented silicon steels," *J. Magn. Magn. Mater.*, vol. 320, no. 7, pp. 1412–1422, Apr. 2008.
- [25] J.-H. Yoo, J. B. Restorff, M. Wun-Fogle, and A. B. Flatau, "Induced magnetic anisotropy in stress-annealed galferol laminated rods," *Smart Mater. Struct.*, vol. 18, no. 10, Oct. 2009, Art. no. 104004.
- [26] L. Daniel, O. Hubert, and M. Rekić, "A simplified 3-D constitutive law for magnetomechanical behavior," *IEEE Trans. Magn.*, vol. 51, no. 3, pp. 1–4, Mar. 2015.
- [27] P. Rasilo et al., "Modeling of hysteresis losses in ferromagnetic laminations under mechanical stress," *IEEE Trans. Magn.*, vol. 52, no. 3, pp. 1–4, Mar. 2016.
- [28] M. Domenjoud, E. Berthelot, N. Galopin, R. Corcolle, Y. Bernard, and L. Daniel, "Characterization of giant magnetostrictive materials under static stress: Influence of loading boundary conditions," *Smart Mater. Struct.*, vol. 28, no. 9, 2019, Art. no. 095012.
- [29] B. J. Mailhé, L. D. Bernard, L. Daniel, N. Sadowski, and N. J. Batistela, "Modified-SST for uniaxial characterization of electrical steel sheets under controlled induced voltage and constant stress," *IEEE Trans. Instrum. Meas.*, vol. 69, no. 12, pp. 9756–9765, Dec. 2020.
- [30] A. Daem, P. Sergeant, L. Dupré, S. Chaudhuri, V. Bliznuk, and L. Kestens, "Magnetic properties of silicon steel after plastic deformation," *Materials*, vol. 13, no. 19, p. 4361, Sep. 2020.
- [31] W. Huang, Z. Tao, P. Guo, B. Wang, and L. Weng, "High-frequency magnetic energy loss based on J-A model for gallium iron alloy rod under variable stress conditions," *J. Magn. Magn. Mater.*, vol. 563, Dec. 2022, Art. no. 169970.
- [32] L. G. D. Silva, A. Abderahmane, M. Domenjoud, L. Bernard, and L. Daniel, "An extension of the vector-play model to the case of magneto-elastic loadings," *IEEE Access*, vol. 10, pp. 126674–126686, 2022.
- [33] B. Toutsop, B. Ducharne, M. Lallart, L. Morel, and P. Tsafack, "Characterization of tensile stress-dependent directional magnetic incremental permeability in iron-cobalt magnetic sheet: Towards internal stress estimation through non-destructive testing," *Sensors*, vol. 22, no. 16, p. 629, 2022.
- [34] I. T. Gürbüz et al., "Experimental characterization of the effect of uniaxial stress on magnetization and iron losses of electrical steel sheets cut by punching process," *J. Magn. Magn. Mater.*, vol. 549, May 2022, Art. no. 168983, doi: 10.1016/j.jmmm.2021.168983.
- [35] M. Domenjoud and L. Daniel, "Effects of plastic strain and reloading stress on the magneto-mechanical behavior of electrical steels: Experiments and modeling," *Mech. Mater.*, vol. 176, Jan. 2023, Art. no. 104510.
- [36] B. Yang, H. Li, and A. Zhang, "Influences of non-coaxial magnetic field on magneto-mechanical effect of ferromagnetic steel," *Int. J. Appl. Electromagn. Mech.*, vol. 59, no. 1, pp. 247–254, Mar. 2019.
- [37] Y. Maeda et al., "Development of the apparatus for measuring magnetic properties of electrical steel sheets in arbitrary directions under compressive stress normal to their surface," *AIP Adv.*, vol. 7, no. 5, May 2017, Art. no. 056664.
- [38] H. Helbling et al., "Effect on magnetic properties of inhomogeneous compressive stress in thickness direction of an electrical steel stack," *J. Magn. Magn. Mater.*, vol. 500, Apr. 2020, Art. no. 166353.
- [39] M. V. Upadhyay, T. Panzner, S. Van Petegem, and H. Van Swygenhoven, "Stresses and strains in cruciform samples deformed in tension," *Experim. Mech.*, vol. 57, no. 6, pp. 905–920, Jul. 2017.
- [40] R. Langman, "Magnetic properties of mild steel under conditions of biaxial stress," *IEEE Trans. Magn.*, vol. 26, no. 4, pp. 1246–1251, Jul. 1990.
- [41] M. J. Sablik, "Modeling the effects of biaxial stress on magnetic properties of steels with application to biaxial stress nde," *Nondestruct. Test. Eval.*, vol. 12, no. 2, pp. 87–102, Jan. 1995.
- [42] M. Rekić, O. Hubert, and L. Daniel, "Influence of a multiaxial stress on the reversible and irreversible magnetic behaviour of a 3%Si-Fe alloy," *Int. J. Appl. Electromagn. Mech.*, vol. 44, nos. 3–4, pp. 301–315, Mar. 2014.
- [43] Y. Kai, Y. Tsuchida, T. Todaka, and M. Enokizono, "Development of system for vector magnetic property measurement under stress," *J. Electr. Eng.*, vol. 61, no. 7, pp. 77–80, 2010.
- [44] U. Aydin et al., "Rotational single sheet tester for multiaxial magneto-mechanical effects in steel sheets," *IEEE Trans. Magn.*, vol. 55, no. 3, pp. 1–10, Mar. 2019.
- [45] Y. Kai, M. Enokizono, and Y. Kido, "Influence of shear stress on vector magnetic properties of non-oriented electrical steel sheets," *Int. J. Appl. Electromagn. Mech.*, vol. 44, nos. 3–4, pp. 371–378, Mar. 2014.
- [46] L. Daniel, "An analytical model for the effect of multiaxial stress on the magnetic susceptibility of ferromagnetic materials," *IEEE Trans. Magn.*, vol. 49, no. 5, pp. 2037–2040, May 2013.

Abdellahi Abderahmane received the Mechanical Engineering degree from Tunis El Manar University, Tunis, Tunisia, in 2016, and the master's degree in acoustical engineering and the Ph.D. degree in electrical engineering from Paris-Saclay University, Paris, France, in 2017 and 2021, respectively.

He is currently a Post-Doctoral Researcher with the Laboratoire de Genie Electrique et Electronique de Paris, Université Paris-Saclay. His research interests include nondestructive testing, tomography imaging, and ferromagnetic materials' characterization.

Laurent Daniel (Member, IEEE) received the Ph.D. degree from the École Normale Supérieure de Cachan, Cachan, France, in 2003, and the Habilitation degree in physics from Université Paris-Sud, Orsay, France, in 2011.

Since 2015, he has been a Full Professor with CentraleSupélec, Université Paris-Saclay, Gif-sur-Yvette, France. His research interests, within the Laboratoire de Genie Electrique et Electronique de Paris, Université Paris-Saclay, are dedicated to electromechanical and magnetomechanical couplings in materials for electrical engineering applications. He is notably involved in the definition of multiscale methods for the prediction of such coupled phenomena and in the development of dedicated experimental characterization setups.